scientific reports

Check for updates

OPEN

Finite element study on the mechanism of the influence of pretension force and block strength on the shear resistance of the anchor cable with C-shaped tube

Renliang Shan[1], Wei Song[1]✉, Shupeng Zhang[2], Xiao Tong[3] & Junqi Liang[1]

To prevent the early breakage of anchor cables under shear loads in support engineering, a combined structure of Anchor Cable with C-shaped Tube (ACC) has been proposed. The shear resistance enhancement mechanism of this structure and the mechanisms of various influencing factors have yet to be fully revealed. A refined nonlinear finite element model of ACC was original established using ABAQUS software, taking into account the actual structure of the steel strands and the interactions, such as contact and failure between the various components. Various anchor cable pretension forces and block strengths were set to investigate their effects on the shear mechanical response of ACC. The results successfully demonstrated a high correlation between peak shear load and pretension force. The results demonstrate that an increase in pretension force reduces the ACC's peak shear load and break displacement. Additionally, the structure exhibited higher flexural stiffness, the block strength was mobilized earlier, and the block failed locally more quickly. Under high pretension forces, the system exhibited higher shear stiffness in the early stages of shearing due to the influence of the axial force component. With low pretension forces, the ACC exhibited a larger break displacement due to the minor tensile deformation at the shear plane position for the same shear displacement. At low pretension forces, the structure's bending angle increased more rapidly during the middle and later stages of shearing, accompanied by a larger break displacement. Both of these factors led to a greater bending angle at the shear plane position at the point of failure. The results reveal the characteristic of the peak shear load initially increasing and then decreasing with the increase in test block strength, along with its underlying mechanism. As the block strength increased, the bending angle of the structure at the shear plane position increased more rapidly, resulting in higher shear stiffness. With high block strength, the combination of smaller break displacement and greater shear stiffness led to an initial increase followed by a decrease in peak shear load. A comprehensive RSSB (Relative Stiffness between Structure and Test Block) that considers both structural and test block stiffness was proposed. The deformation pattern of the structure was controlled by the RSSB. The higher the RSSB, the wider the plastic hinge extension range for the same shear displacement, the smaller the bending angle at the shear plane position, and the smaller the maximum curvature of the structure. The contact force of the C-shaped tube generally exhibited a "single peak" distribution. As the shear displacement increased, the peak position of the contact force moved away from the shear plane, and the maximum contact force increased rapidly and remained relatively stable. At the end of the shearing process, the contact force of the C-shaped tube exhibited a "double peak" distribution.

Keywords Support engineering, Anchor cable with C-shaped tube, Double shear test, Nonlinear finite element method, Pretension force, Test block strength

[1]School of Mechanics and Civil Engineering, China University of Mining and Technology (Beijing), Beijing 100083, China. [2]North Blasting Technology Co., Ltd., Beijing 100097, China. [3]School of Earth Science and Engineering, Hebei University of Engineering, Handan 056038, China. ✉email: bqt2000604044@student.cumtb.edu.cn

Anchor cables, commonly used as reinforcement components in tunnel and slope engineering, have been characterized by their high load-bearing capacity, significant anchorage depth, and the ability to apply substantial pretension forces. In China's coal-bearing strata, typical layered structures are commonly present. After tunnel excavation and face mining, the surrounding rock is prone to delamination and fracturing under disturbance. The interlayer structural planes will likely undergo mutual dislocation, causing support components such as anchor cables to be subjected to lateral loads. Under lateral loads, these support components are prone to breakage and failure, adversely affecting engineering safety[1–3]. The Anchor Cable with C-shaped tube (ACC) is a novel support structure proposed against this engineering backdrop[4,5]. The anchor cable with C-shaped tube (ACC) is composed of a C-shaped slotted steel tube combined with an anchor cable. This design changes the contact state between the free section of the anchor cable and the surrounding rock, thereby enhancing the structure's resistance to lateral loads while maintaining the axial resistance of the anchor cable.

Many scholars have studied the reinforcement mechanisms of support components on the surrounding rock. Kang et al.[6] conducted tensile tests on several commonly used steel strands for anchor cables in coal mines to determine their basic tensile properties and pointed out that underground anchor cables endure a complicated stress state due to the combined effects of tensile, shear, and bending forces. Hence, it is crucial to develop testing equipment capable of assessing the mechanical properties of anchor cables under various stress conditions to thoroughly comprehend the mechanisms behind their deformation and failure. Aziz et al.[7] investigated the effect of various factors on the shear mechanical properties of fully grouted anchor cables through single shear tests. These factors included anchor cable type, pretension force, surface profile type, shear load application rate, and debonding. They observed that increasing the pretension force of the anchor cable reduces the peak shear load. Yang et al.[8] explored the influence of surrounding rock strength, pretension force, and anchoring method on the shear capacity of anchor cables through double shear tests, revealing that a reduction in the strength of the test block mortar led to an increase in the anchor cable's peak shear load. Furthermore, the break displacement of the anchor cable diminished as the pretension force augmented. The anchor cable's initial shear stiffness increases with greater pretension force, while the later shear stiffness remains relatively unchanged. Chen et al.[9], based on the variational principle of minimum potential energy and the Pellet model, established a calculation formula for the shear strength of anchored structural planes, considering the dilatancy of the structural planes, and solved the governing equations using numerical methods and pointed out that during the shearing of jointed rock masses, the contribution of the anchor rods' shear force to the overall shear strength is significant and cannot be overlooked. Liu et al.[10] conducted indoor shear tests on jointed rock masses with different anchor rod inclinations and normal stress levels and pointed out that within a specific range, increasing the strength of the anchor rods results in higher shear strength of the anchored jointed rock masses. In addition, the mechanism of rock reinforcement with anchor rods was discussed based on the shear load-displacement curves. Wang et al.[11] thoroughly considered the setting of the anchoring end and conducted similar simulation single shear tests. Contributions of dowel action, prestress, and axial force increment to shear resistance were studied and several valuable conclusions were provided: (1) Increasing the pretension of the anchor cable enhanced the initial stiffness in the shear load-displacement curve. (2) In the initial stage of shear displacement, pretension and dowel action plays a major role. Simultaneously, the increase in axial force plays a crucial role once plastic hinges form in the rod body. The failure of the anchor cable generally occurs near the joint surface, belonging to a combined tensile-shear failure mode. Song et al.[12] examined the effect of both normal stress and rock strength in similar direct shear tests. The findings revealed that as the installation angle of the anchor rod increased, its axial force contributed less to shear resistance. In contrast, the contribution of the shear force of the anchor rod to shear resistance increased. Zhang et al.[13] investigated the shear behavior of anchor rods made from basalt fiber-reinforced polymer (BFRP). The evidence suggested that the failure of BFRP was mainly due to the failure of the resin matrix and basalt fibers. Compared to steel anchor rods, the shear break displacement of BFRP was smaller, and there was no obvious plastic hinge extension. Wang et al.[14] performed single-shear tests on fully grouted anchor cables utilizing a large-scale testing apparatus. A detailed model of the steel strands of the anchor cables was established using ABAQUS software to perform finite element simulations of the experimental results. According to the numerical simulation results, notable compressive stress was present locally at the test block's shear interface. Faham et al.[15,16] have investigated the shear mechanical properties of support members under static and dynamic loads, as well as the effects of anchor cable diameter and strength on their shear performance. Ma et al.[17] proposed a theoretical model for the shear load-displacement curve of anchor rods applicable to both double-shear and single-shear tests. Grounded in the elastic foundation beam theory, this model accounted for the reduction in foundation stiffness caused by surrounding rock fracturing and the extent of plastic hinge distribution. The model was validated against experimental data. Jiang et al.[18] designed direct shear tests to study the shear performance of anchor rods using normal stiffness boundary conditions. The research results showed that increasing the normal stiffness of the joint surface led to a corresponding increase in the strength of the locally anchored material, while causing a decrease in the plastic hinge extension range of the anchor rod. The anchor rod's failure mode shifted from tensile failure to bending-shear failure. Shan et al.[19] studied the shear performance of ACC through double shear tests and investigated the failure modes of anchor cables and ACC and the influence of pretension force. Tong et al.[20] studied the effects of C-shaped tube strength and normal stress on the shear characteristics of ACC. Related studies on the mechanical characteristics of the anchor cable with C-shaped tube (ACC) structure have been conducted[21–24], and this combined structure has already been successfully applied in several mines.

Previous studies have predominantly focused on the shear mechanical properties of anchor rods or cables, with research on the novel composite structure of ACC remaining scarce. As a composite structure, ACC exhibits distinct mechanical characteristics compared to anchor cables or rods. The investigation into its shear mechanical behavior, particularly under varying pretension forces and test block strengths, along with the underlying shear resistance mechanisms, remains largely unexplored or severely underrepresented, necessitating

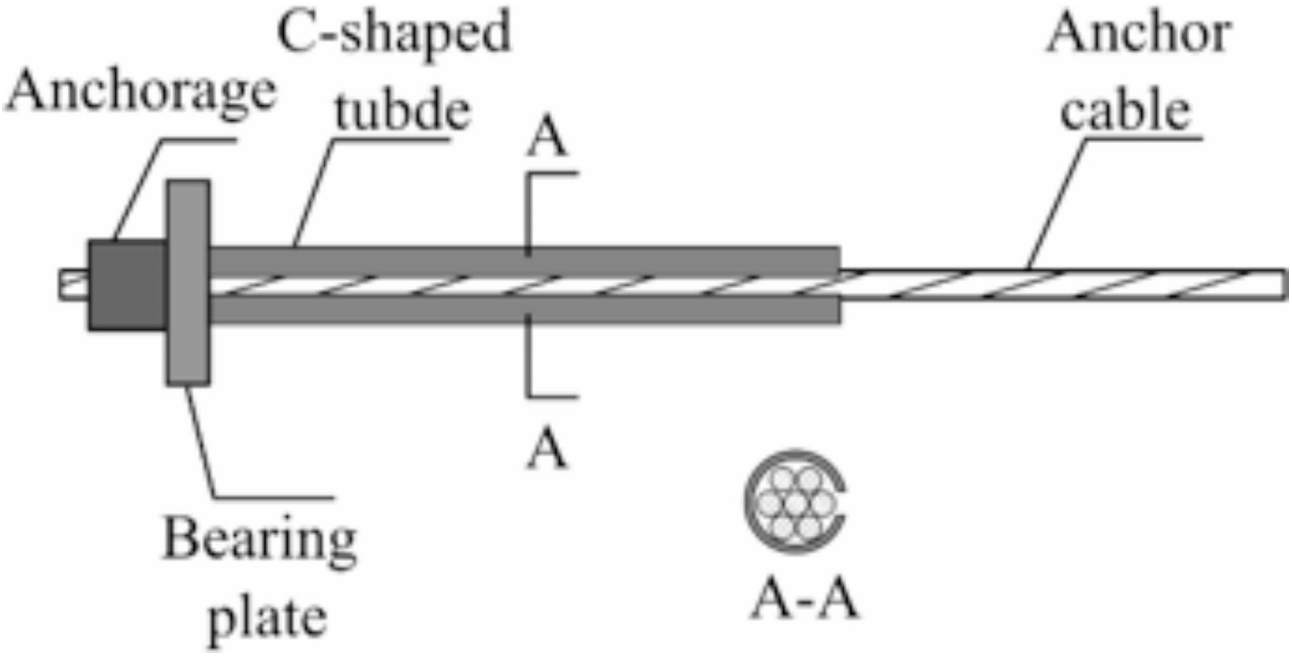

Fig. 1. Schematic diagram of the ACC structure.

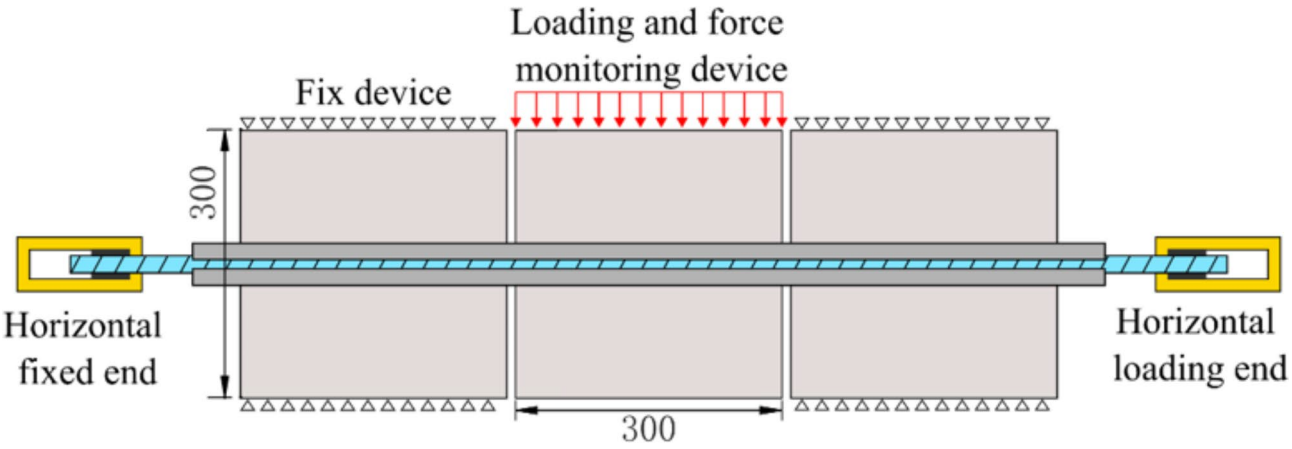

Fig. 2. Overall schematic diagram of double shear test.

urgent research efforts.Furthermore, in the current studies examining the shear mechanisms of anchor rods and cables, most research merely presents the quantitative relationships between different physical physical quantities, without fully elucidating the mechanisms behind these relationships. High-precision numerical simulations that align well with experimental results, offering valuable insights into the mechanisms, are notably rare. Consequently, there is a pressing need to address this gap in the literature. Therefore, the mechanisms by which various influencing factors affect this combined structure's shear resistance and failure process still need further research. Based on existing double shear tests, this study investigates the influence mechanisms of block strength and anchor cable pretension on the shear performance of ACC using the finite element method.

Numerical model setup and parameter selection for ACC double shear tests

The ACC is formed by the anchor cable and the C-shaped slotted steel tube. The basic structure, as shown in Fig. 1. The mechanical performance of this structure can be tested and studied through double-shear tests. For detailed information on the specific composition of ACC and the double shear test procedure, refer to the literature[17]; thus, it will not be elaborated here.

Numerical model, boundary conditions, and material settings

The overall model of the double-shear test is depicted in Fig. 2 Prior to the test, cubic test blocks with a side length of 300 mm and a central circular hole of 32 mm in diameter were cast using molds. After curing, the

Block		Cable		C-shaped tube	
Side length	300 mm	Diameter	21.6 mm	Inner diameter	24 mm
Opening diameter	32 mm	Length	1.2 m	Outer diameter	28 mm
		Form	1×7	Slot width	8 mm

Table 1. Geometric dimensions of the model.

		Contact method	
Contact part 1	Contact part 2	Normal direction	Tangential friction coefficient
Metal wire	Metal wire	Hard contact	0.15
Cable	C-shaped tube	Hard contact	0.15
C-shaped tub	Block	Hard contact	0.2
Block	Block	Hard contact	Frictionless

Table 2. Settings of contact relationship.

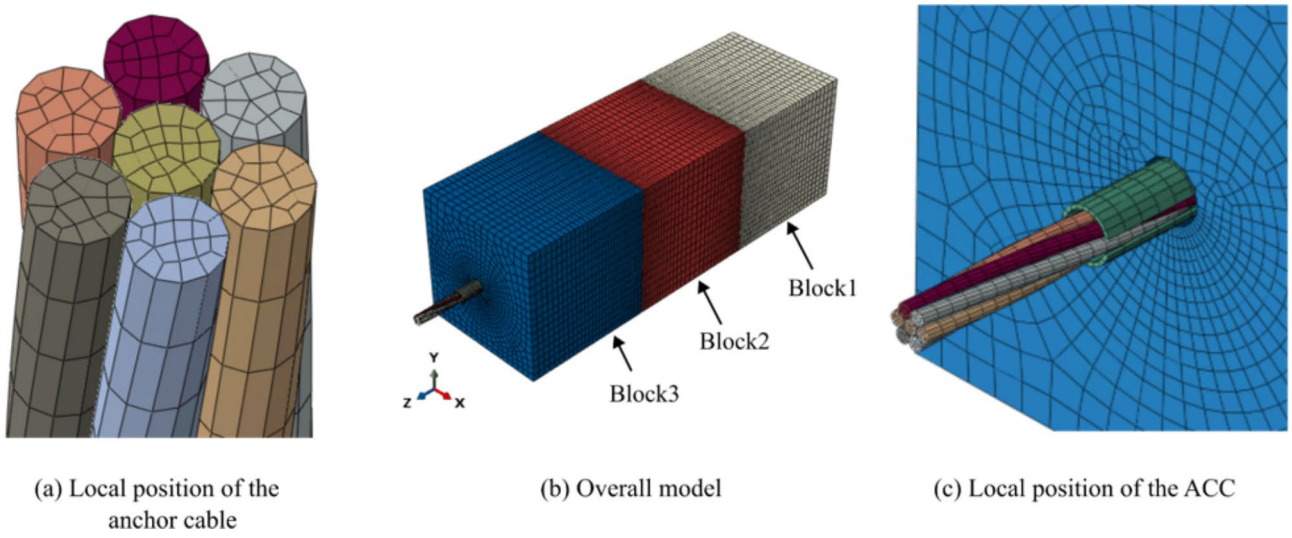

(a) Local position of the anchor cable (b) Overall model (c) Local position of the ACC

Fig. 3. Numerical calculation model of double shear test and elements mesh.

component was inserted into the hole of the test block, and three test blocks were then moved to the designated position of the test using lifting equipment. The loading phase commenced by first applying a pretension force to the anchor cable up to a specified value, followed by the fixation of both ends of the anchor cable. Vertical shear loads were then imposed until the component ruptured. Finally, the test blocks were removed, and the failure modes were recorded. To delve deeper into the shear mechanism of the ACC and compare it with experimental outcomes, a finite element model was created using ABAQUS software, taking the double shear test as a reference. The geometric parameters were selected according to the actual double shear test, and the parameter values are shown in Table 1. The contact settings between the various components are detailed in Table 2. In the double shear test, the ends of the anchor cable were fixed to the frame using anchorage. In the numerical model, nonlinear springs were set at both ends of the anchor cable to simulate the anchoring characteristics of the anchorage. The numerical simulation model is shown in Fig. 3[19]. The model used C3D8R elements for all units, comprising 153,691 elements. Parallel solving was utilized for the calculations. For additional detailed parameters, refer to the literature[19].

Numerical test scheme

During the double shear test, the pretension forces were set to 100 kN, 200 kN, and 300 kN. The test blocks were made of cast concrete, with strengths of 20 MPa, 40 MPa, and 50 MPa. To study the mechanisms by which anchor cable pretension force and test block strength influence the shear performance of ACC, and considering the existing double shear test results and research objectives, Several combinations of different anchor cable pretension forces and test block strengths were established in the numerical simulation. The anchor cable used was a 1×7 structure with a diameter of 21.6 mm steel strand. The numerical test set the anchor cable pretension

forces at four levels: 0 kN, 100 kN, 200 kN, and 300 kN. The test block strength was set at five levels based on uniaxial compressive strength: 20 MPa, 30 MPa, 40 MPa, and 50 MPa.

The elastic modulus of concrete for various strengths was determined using the formula mentioned in literature[25], as shown in Eq. (1). The tensile strength was determined using the formula mentioned in the literature[26], as shown in Eq. (2). The Poisson's ratio was uniformly set to 0.2.

$$E_c = \frac{10^5}{2.2 + 34.74/f_{cu}}, \tag{1}$$

where f_{cu} is the cubic compressive strength of the concrete, measured in MPa.

$$f_t = 0.26\, f_{cu}^{2/3}, \tag{2}$$

where f_t is tensile strength, measured in MPa.

Analysis of shear mechanical properties and influencing factors of ACC

This section first briefly analyzes the mechanical response of ACC under shear loading. Subsequently, numerical experiments are conducted according to the pretension force levels and test block strength grades set in Subsection "Numerical test scheme". The computational results are then compared with the experimental results, with a focus on analyzing the mechanical response of both the structure and the test block. The primary objective is to clarify the differences in the mechanical response of ACC structures under varying pretension forces and test block strengths, as well as the underlying mechanisms that give rise to these differences. This analysis aims to deepen the understanding of the shear resistance mechanisms of support members.

Mechanical response of ACC shearing

The interface between the test blocks is called the test block interface. When the ACC is subjected to shear at the test block interface, this interface is referred to as the shear plane in the analysis of the ACC's mechanical response. In the numerical simulation, a monitoring point was set at the top of Test Block 2 to monitor the force and displacement on the top surface. The monitored vertical force is called the shear load in the following text. The shear load-displacement curve derived from the numerical simulation was contrasted with the experimental curve, as illustrated in Fig. 4. The overall shear process was divided into several stages. There was a gap between the C-shaped tube and the wall of the test block hole. In the initial shearing stage, there was no contact between the test block and the structure; this phase was identified as the no-contact stage, where the axial force stayed at the pretension force, and the shear load was nearly zero. As the shear load increased, the test block came into contact with the ACC, and the shear load was borne by the ACC as a whole. The shear load increased with the shear displacement. It suddenly dropped after reaching the peak shear load, indicating that the anchor cable had broken. As illustrated in Fig. 4, the numerical simulation results closely matched the experimental results, indicating that this numerical model could effectively reflect the overall process of stress and deformation of the ACC.

The deformation process of the ACC under shear load is shown in Fig. 5, and the stress deformation mode of the ACC under shear load is shown in Fig. 6. In the initial shearing stage, the ACC underwent bending deformation and formed plastic hinges under shear force and bending moment symmetrically distributed along the shear plane. As the shear load increases, the concrete at the test block interface locally fractured, and the plastic hinges extended away from the test block interface. The deformation of the ACC was composed of symmetrically distributed bending deformation at the shear plane and tensile deformation in the middle section of the structure. As the shear load increased, the test block's damage and failure area gradually expanded. The compressive damage in the CDP model could characterize this mechanical process well. After the experiment, the shape of the test block and the distribution of compressive damage obtained from numerical simulation are shown in Fig. 7. The white powder formed after the local microscopic fragmentation of the test block under high compressive stress was essentially consistent with the higher range of compressive damage obtained from numerical simulation.

Due to its helical structure, the anchor cable experienced varying degrees of deformation among its metal wires under overall shear loading, and this bending deformation is dependent on their spatial positions. As the shear displacement increased, the evolution of axial forces in different metal wires at various positions on the shear surface is illustrated in Fig. 8. It was noted that the initial axial forces of different metal wires varied slightly, and their subsequent evolution of axial forces was also inconsistent. The rate of axial force growth was related to the bending radius of the metal wire; the more significant the bending radius, the faster the axial force increased. At the point of ultimate failure, the axial forces in the metal wires remained different. Some individual metal wires (such as #7) experienced a certain degree of unloading in the initial shearing stage due to their geometric position, leading to a decrease in axial force to some extent.

The above analysis indicates that the nonlinear finite element model established using ABAQUS could effectively simulate the mechanical response of ACC during shear loading. This model enabled the investigation of the shear mechanical properties of ACC under various block strengths and anchor cable pretension forces.

The influence of pretension force on the shear properties of ACC

The relationship between the maximum Mises stress of the anchor cable and the pretension force after the tensioning process is illustrated in Fig. 9. It is evident that the maximum Mises stress increased approximately linearly with the pretension force. The Mises stress distribution at the central cross-section of the anchor cable during the tensioning stage under different pretension forces is shown in Fig. 10. As the pretension force

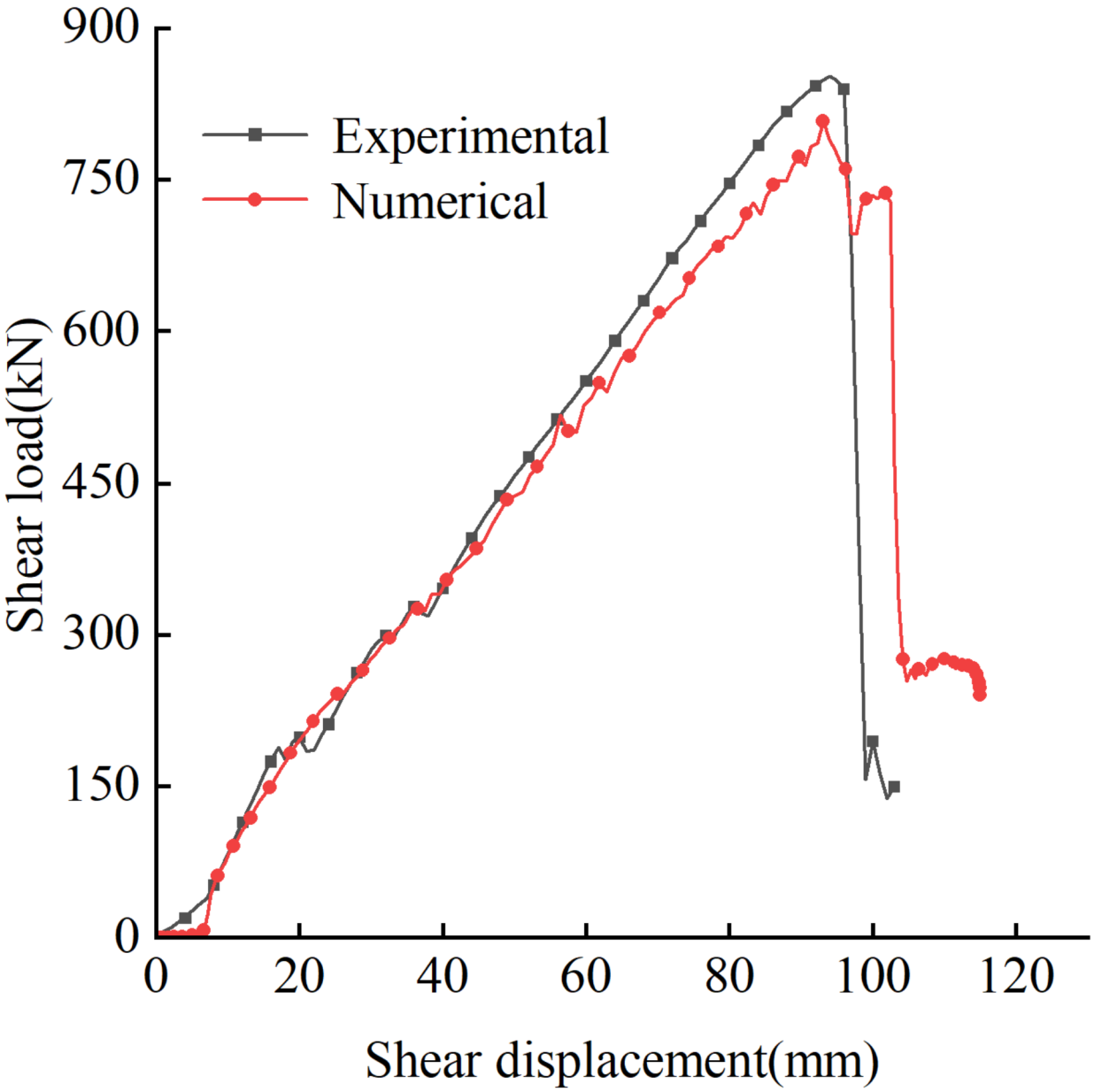

Fig. 4. Contrast of shear load versus shear displacement curves.

increased, the overall Mises stress rose. Due to the helical geometry of the anchor cable, there was a coupling of tensile and bending deformations in the individual metal wires under tensile load, resulting in a non-uniform stress distribution. However, the stress distribution exhibited a certain degree of symmetry.

Under shear loading, the ACC underwent bending deformation on both sides of the shear plane. According to Liu et al.[27], it was noted that both the axial and shear forces of the support components at the shear plane contributed to resisting the shear load. The middle section of the double shear system was analyzed for its force, as shown in Fig. 11a. The calculation of the shear load in the double shear system is given by Eq. (3). The resultant force was doubled since there were two shear planes in the double shear test.

$$F_v = 2\left(F_n \sin\theta + F_s \cos\theta\right), \tag{3}$$

where F_v is the shear load, F_n is the axial force at the shear plane position, F_s is the shear force at the shear plane position, θ is the bending angle of the structure.

Using the free body cut feature in ABAQUS, the axial force, shear force, and bending angle at the shear plane position of ACC were extracted. The calculated results of Eq. (3) were compared with the simulated shear load-

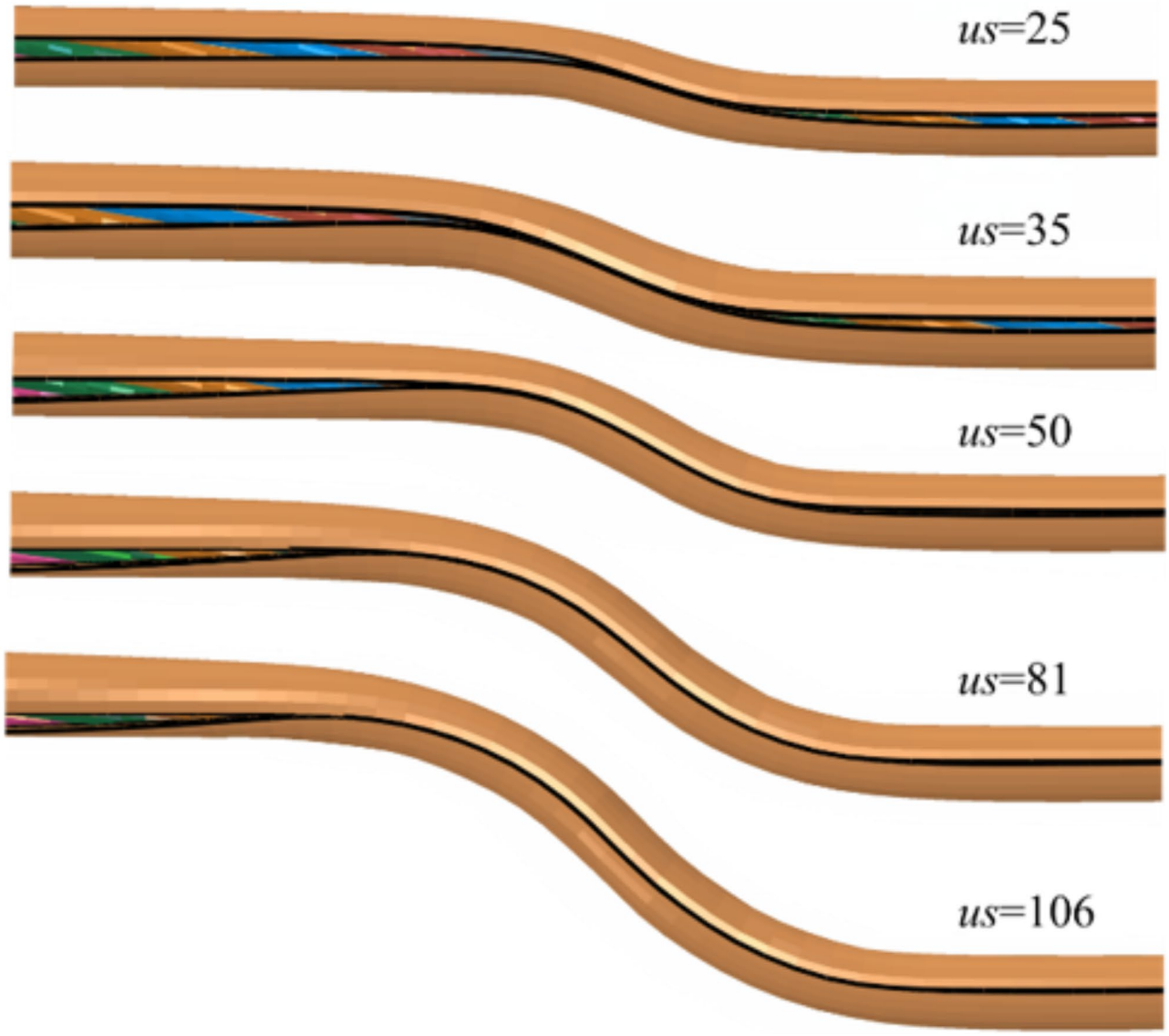

Fig. 5. Deformation process of ACC subjected to shear load *(us* denotes the shear displacement).

displacement curve, as illustrated in Fig. 11b. The two curves are essentially consistent, indicating that Eq. (3) can reflect the force characteristics of the shearing process.

The test block strength was set to 40 MPa. Table 3 shows the peak shear load and break displacement values of the ACC under different pretension forces. The numerical simulation results were compared with the experimental results, as shown in Fig. 12a and b. The numerical simulation results and the experimental results exhibited the same trend: as the pretension force increased, the break displacement of the anchor cable decreased, and the peak shear load reduced.

Under different pretension forces, the relationship between the ACC inclination at the shear plane and the shear displacement is shown in Fig. 13. The bending angle of the structure evolves in a similar manner under varying pretension forces. With increasing shear displacement, the bending angle also increased, but the rate of this increase gradually decelerated. When the shear displacement was less than 28 mm, the evolution of the bending angle under different pretension forces showed no significant difference. After this point, the bending angle increased rapidly under lower pretension forces. When the shear displacement was less than 28 mm, it was primarily the stage of plastic hinge formation. The structure underwent symmetrical bending deformation on both sides of the shear plane, as shown in Fig. 14. Chen et al.[28] pointed out that the higher the pretension force, the greater the bending stiffness of the steel strands. Therefore, the higher the pretension force, the greater the overall bending stiffness of the ACC. At a shear displacement of 28 mm, the distribution of the minimum principal stress in the test block under different pretension forces is shown in Fig. 15. It is observed that, at a pretension force of 300 kN, the absolute value of the minimum principal stress was greater at the contact points between the test block and the structure. The test block, being locally subjected to triaxial compression, had a

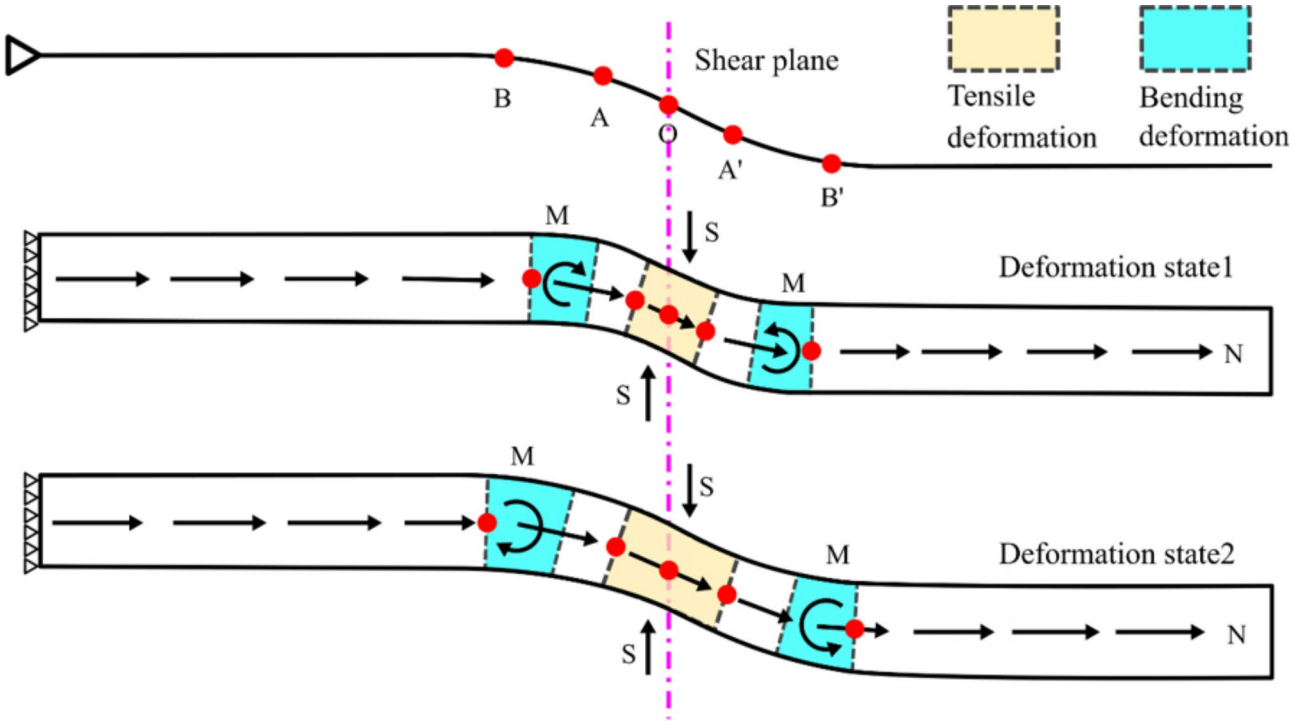

Fig. 6. The force and deformation model of ACC (M represents bending moment, S represents shear force, N represents axial force, right is the positive direction of cross-section).

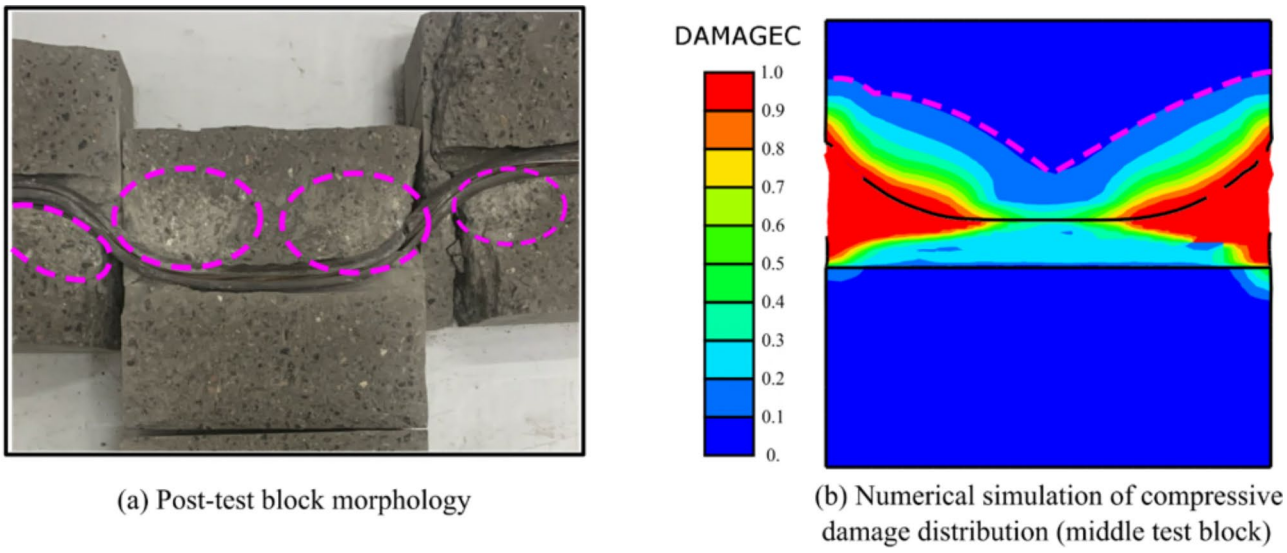

(a) Post-test block morphology

(b) Numerical simulation of compressive damage distribution (middle test block)

Fig. 7. The shape and damage distribution of the block after double-shear testing.

specific load-bearing capacity. Under a pretension force of 300 kN, due to the higher stiffness of the structure, the strength of the test block was mobilized earlier, and it reached the failure condition sooner. This resulted in the local crushing of the test block, with the plastic hinge simultaneously extending outward and the bending deformation of the structure further increasing. At a shear displacement of 61 mm, the deformation patterns of the structure under various pretension forces were compared, as shown in Fig. 16. Under identical shear displacement, the higher the pretension force, the smaller the bending angle of the structure at the shear plane position. The schematic diagrams of the bending patterns of the structure under different pretension forces are shown in Fig. 17, where u_s represented the shear displacement. In the plastic hinge extension stage, where the shear displacement was greater than 28 mm, the higher the pretension force, the smaller the bending angle of the structure at the shear plane position, and the larger the lateral extension distance of the plastic hinge. This is consistent with the evolution pattern of the bending angle shown in Fig. 13 .

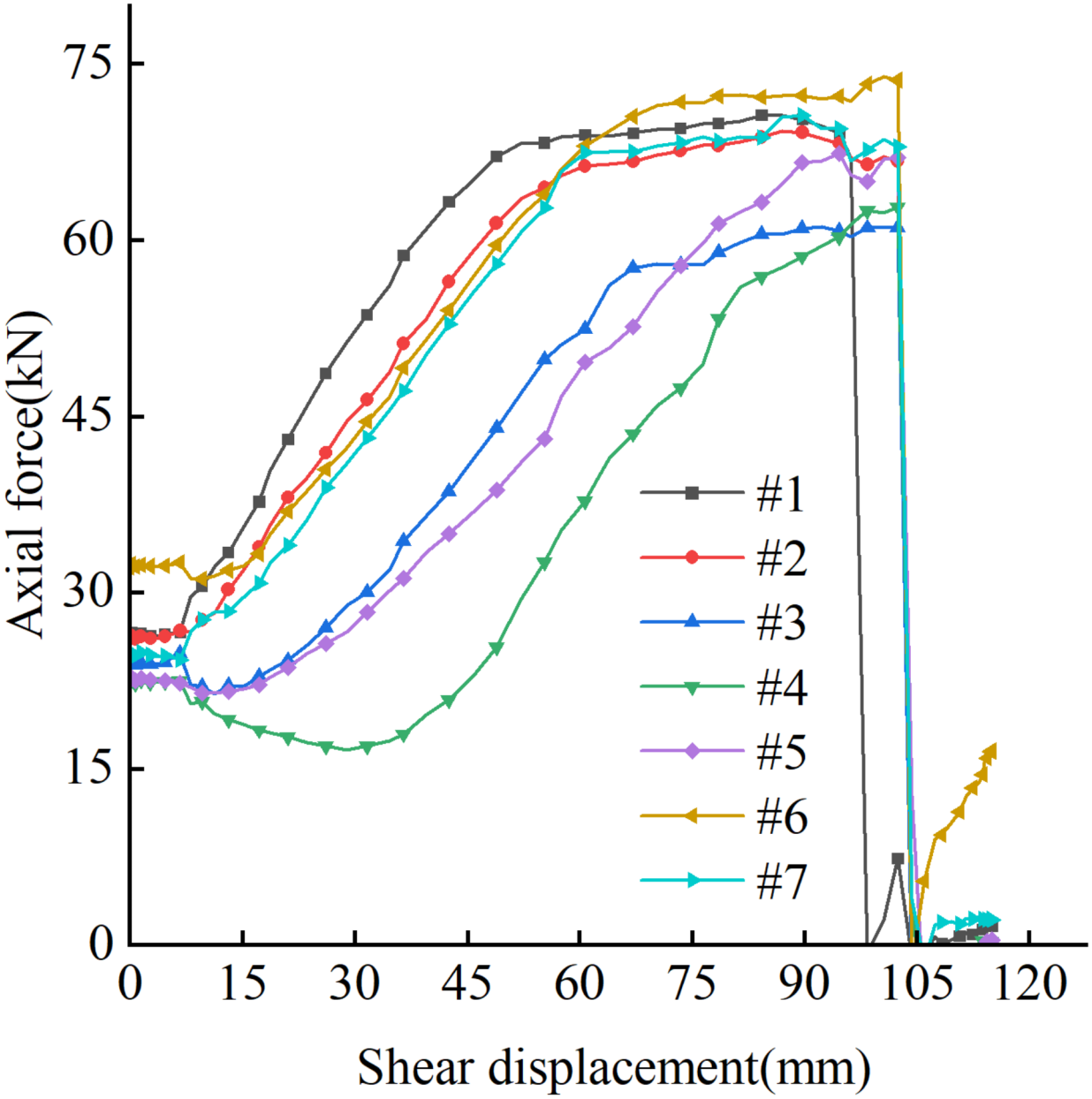

Fig. 8. The evolution of axial forces in each metal wire at the shear plane.

Overall, the tensile deformation of the anchor cable consisted of the tensile deformation caused by applying the pretension force and the subsequent local tensile deformation caused by the shear load. The influence of pretension force on the break displacement had two aspects. Firstly, the higher the pretension force, the greater the overall tensile deformation of the anchor cable before the shear began, resulting in more significant tensile deformation at the shear plane position for the same displacement. On the other hand, as shown in Fig. 17, the deformation pattern of the structure under high pretension force led to reduced tensile deformation of the anchor cable at the shear plane position. However, the initial tensile deformation of the anchor cable still played a controlling role, thus the break displacement decreased with higher pretension forces.

The variation of the maximum bending angle of the ACC with pretension force is shown in Fig. 18, and the experimental results are illustrated in Fig. 19[29]. The maximum bending angle of the structure decreases as the pretension force increases. Under low pretension force, the ACC exhibited a rapid increase in bending angle in the middle and later stages of shearing, and the break displacement of the ACC was larger. These two factors combined to result in a larger bending angle at the shear plane position at the point of failure under low pretension force.

The evolution of ACC's shear force at the shear plane position under different pretension forces is shown in Fig. 20a. When the shear displacement was less than 28 mm, the shear force under different pretension forces

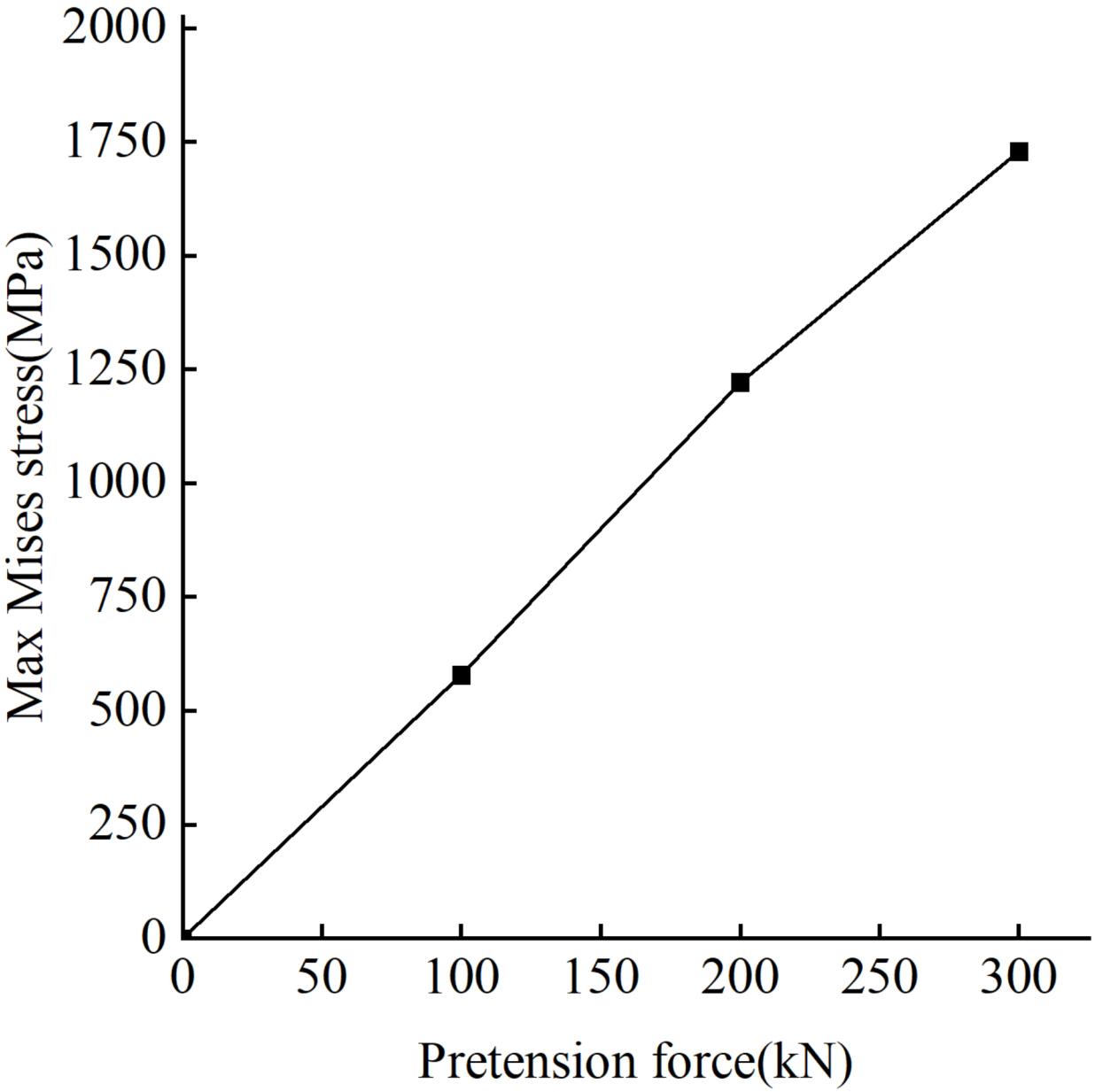

Fig. 9. Maximum Mises stress in the anchor cable during the tensile stage under different pretension forces.

increased rapidly. The peak shear force at 0 kN pretension was slightly lower, and the displacement corresponding to the peak shear force increased. Under different pre-tensioning forces, the maximum shear force reached approximately 60 kN, with only minor differences. After that, as the shear displacement increased, the shear force gradually decreased and fluctuated within a specific range. The evolution pattern of shear force also indicated that when the shear displacement was less than 28 mm, it was primarily the plastic hinge formation stage. During this stage, the ACC had high bending stiffness, resulting in a rapid increase in shear force. After the plastic hinge formed, the bending stiffness of the structure decreased rapidly, and the contact area between the structure and the test block increased. The contact force between the test block and the structure then drove the subsequent bending deformation. Under a pretension force of 200 kN, the evolution of the shear force between the anchor cable and the C-shaped tube at the shear plane position is shown Fig. 20b. The evolution pattern of the shear force between the anchor cable and the C-shaped tube was consistent with that of the ACC. When the shear force reached its peak, the shear force of the C-shaped tube accounted for approximately 30% of the ACC's shear force. The C-shaped tube bore part of the shear load, allowing the anchor cable's strength to be better utilized.

The shear load-displacement curves under different pretension forces are compared in Fig. 21a. The slope of the curve is defined as the shear stiffness of the system. Under high pretension force, the system exhibited

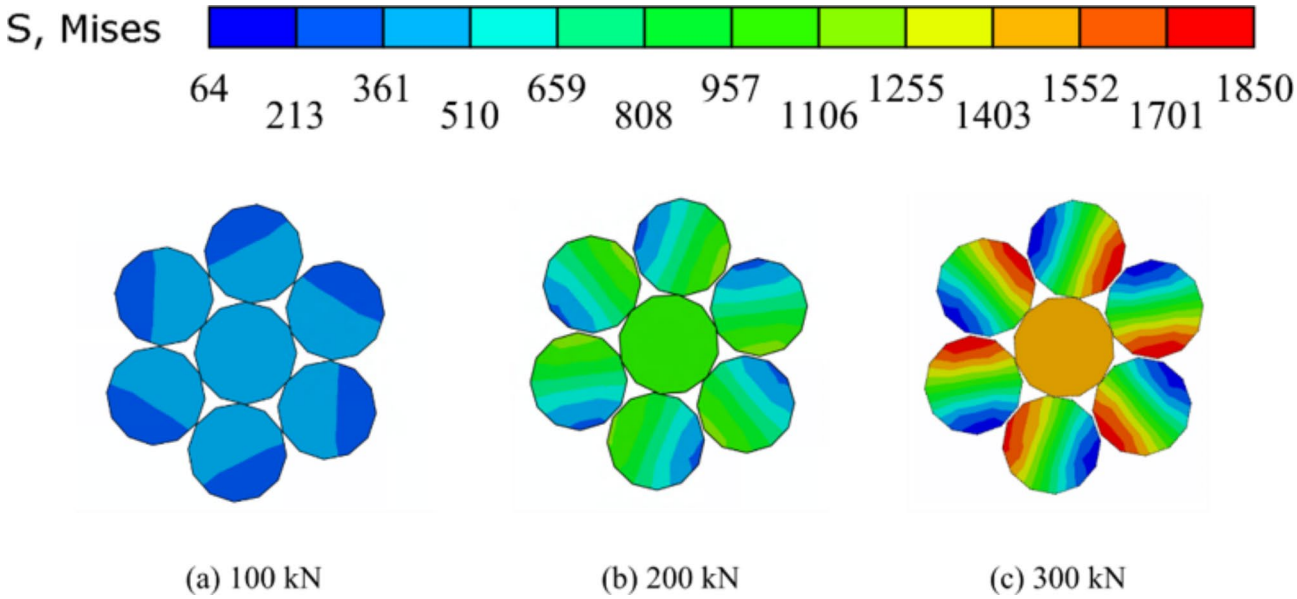

Fig. 10. Distribution of Mises stress in the anchor cable during tensile stretching under different levels of pretension.

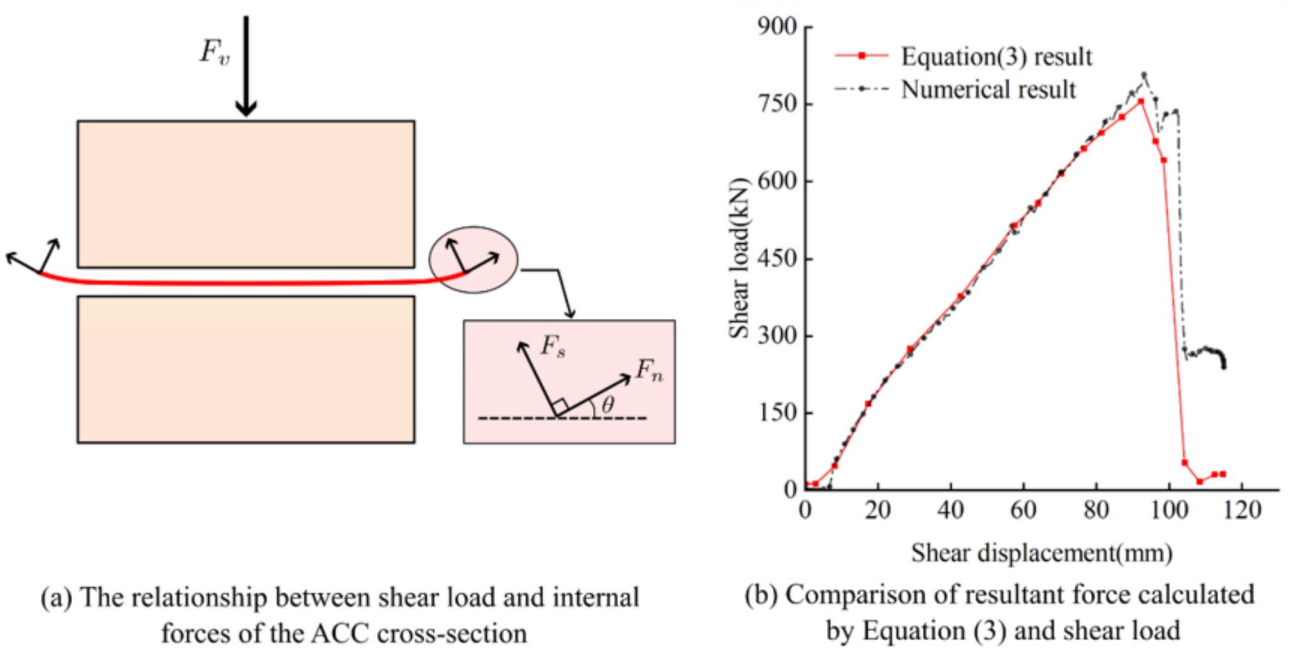

Fig. 11. The relationship between the system shear load and the internal forces within the ACC cross-section.

Pretension force (kN)	Peak shear load (kN)	Peak axial force (kN)	Break displacement (mm)
0	879.44	480.43	123.21
100	842.23	483.49	104.84
200	808.32	491.96	96.25
300	774.73	496.22	93.09

Table 3. Comparison of shear resistance performance of ACC under different pretension forces.

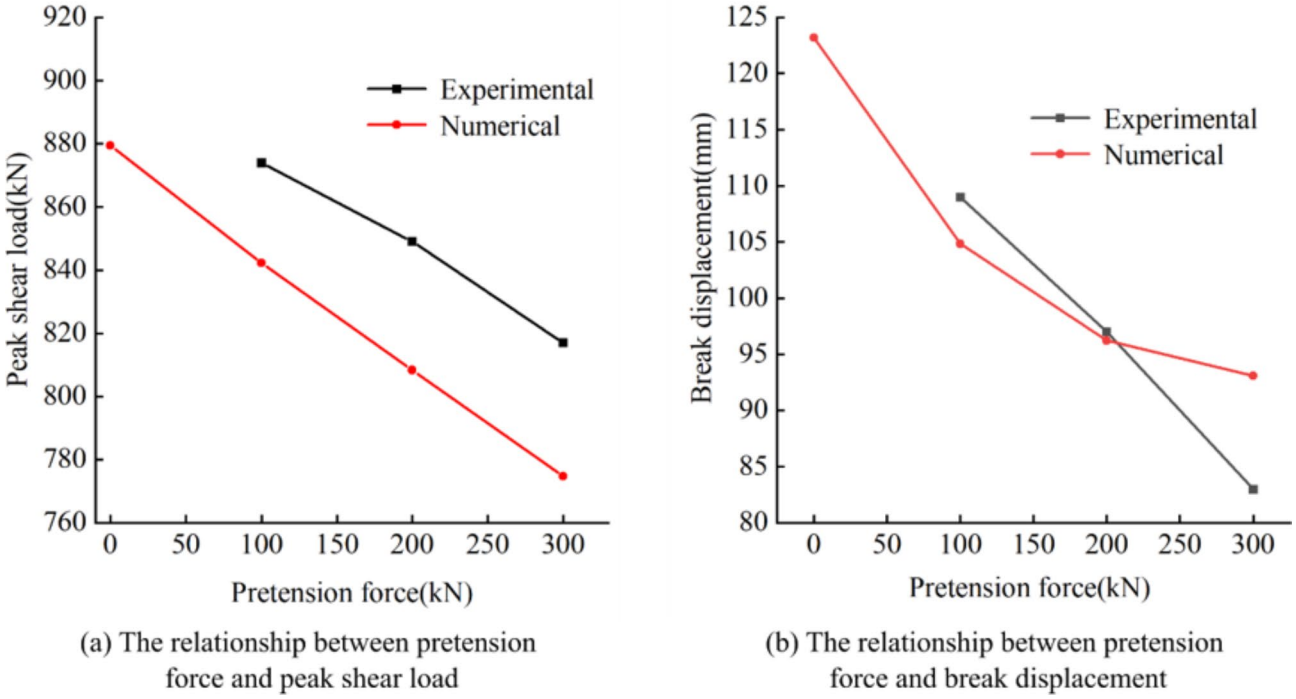

(a) The relationship between pretension force and peak shear load

(b) The relationship between pretension force and break displacement

Fig. 12. Influence of pretension force on the shear resistance of ACC.

higher shear stiffness in the initial shearing stage, with the shear load increasing more rapidly. When the shear displacement exceeded 45 mm, the differences in shear stiffness among the systems under different pretension forces were minimal. The axial force-shear displacement curves under different pretension forces are shown in Fig. 21b. With the increase in shear displacement, the axial force exhibited the same pattern of change: it increased rapidly in the initial stage of shearing, and then the rate of increase slowed down in the later stage. By taking the total differential of Eq. (3), the differential relationship was obtained, as shown in Eq. (4).

$$\mathrm{d}F_v = 2\left(\mathrm{d}F_n \sin\theta + \mathrm{d}F_s \cos\theta + \mathrm{d}\theta\left(F_n \cos\theta - F_s \sin\theta\right)\right). \tag{4}$$

The initial value of the system shear load under different pretension forces was 0. The difference in shear load increments led to different shear stiffness in the shear load-displacement curves under different pretension forces. Differences in the shear force, axial force, and structural angle at the shear plane position all contributed to the differences in system shear load. When the shear displacement was less than 45 mm, the difference in system shear stiffness under different pretension forces was mainly caused by the difference in axial force. As the shear load increased, the difference in structural axial force under different pretension forces decreased. Since the differences in shear force and bending angle at the shear plane position were insignificant, the difference in system shear load under different pretension forces gradually diminished.

The influence of test block strength on the shear properties of ACC

At a pretension force of 200 kN, the peak shear loads under different test block strengths are compared in Fig. 22a. As the test block strength increased, the peak shear loads first increased and then decreased. The break displacements of ACC under different test block strengths are compared in Fig. 22b. As the test block strength increased, the break displacement of the ACC decreased. The experimental results of ACC shear load evolution under different test block strengths are shown in Fig. 23a[29], and the simulation results are shown in Fig. 23b. The experimental results and the simulation results exhibited good consistency. Overall, the higher the test block strength, the greater the shear stiffness of the system. In the initial shearing stage, the shear stiffness was at its maximum for all test block strengths.With the rise in shear displacement, the system's shear stiffness diminished. As the test block strength decreases, the reduction in shear stiffness becomes more significant in the middle and later stages of shearing.

The evolution of ACC axial force under different test block strengths is shown in Fig. 24. ACC axial force was essentially consistent across different test block strengths. The higher the test block strength, the faster the axial force increased, but the differences were relatively small. In the initial shearing stage, the axial force maintained a steady increase. In the later stage, the rate of increase significantly slowed down. Due to the influence of the break displacement, the lower the test block strength, the more extensive the shear displacement range during the slow growth phase of the axial force. The evolution of shear force at the shear plane position for structures with different test block strengths is shown in Fig. 25a. As the shear displacement increased, the shear force at the shear plane position of the ACC initially increased rapidly, then gradually decreased, and finally stabilized

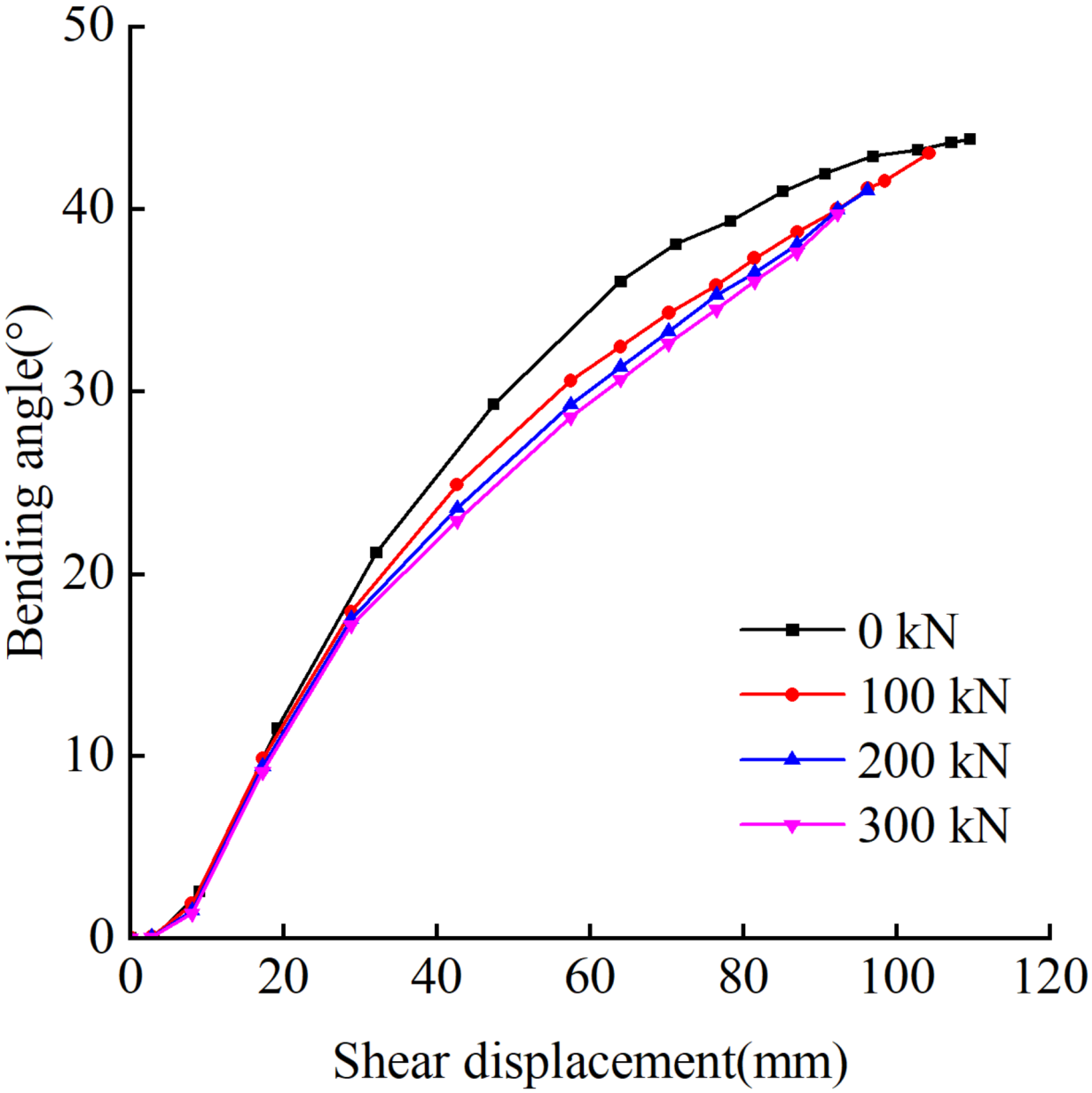

Fig. 13. The relationship between the bending angle and shear displacement of ACC under different pretension forces.

within a specific range. The peak shear forces at the shear plane position for structures with different test block strengths are shown in Fig. 25b. As the test block strength increased, the peak shear force at the shear plane position also increased. In the initial shearing stage, the local concrete at the test block interface was in a triaxial compression state. The higher the test block strength, the greater its load-bearing capacity. Consequently, the reaction force applied to the structure through contact was higher. Under the antisymmetric distribution of reaction forces on both sides of the shear plane, the resulting shear force in the structure was also higher.

The numerical simulation results indicated that the axial force at the shear plane position was essentially consistent with the axial force at the end. The evolution of axial force was essentially consistent across different test block strengths, with only slight differences in shear force at the shear plane position. The evolution of the bending angle at the shear plane position for structures with different test block strengths is shown in Fig. 26. The higher the test block strength, the faster the bending angle at the shear plane position increased. Combined with Eq. (3) the rapid increase in the bending angle was the reason for the higher shear stiffness of the system. At the same time, influenced by the larger break displacement under lower test block strength, the difference in the bending angle at the shear plane position at the final failure point was insignificant. At a shear displacement of 74 mm, the deformation patterns of the ACC at the shear plane position for different test block strengths

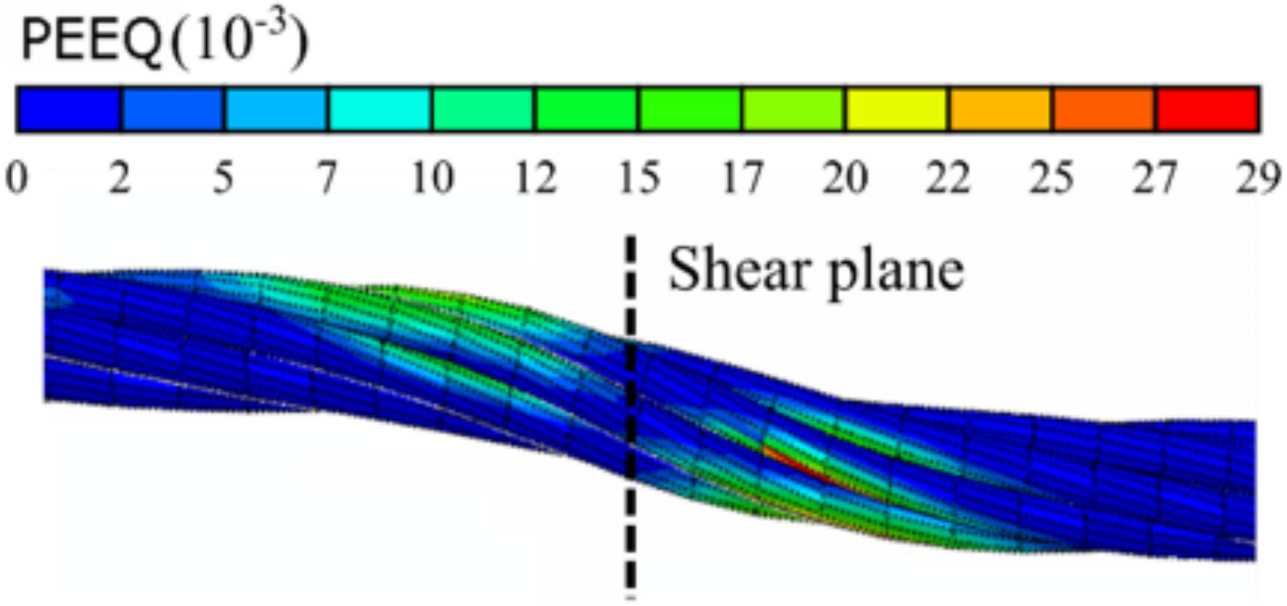

Fig. 14. Symmetric bending deformation of the anchor cable.

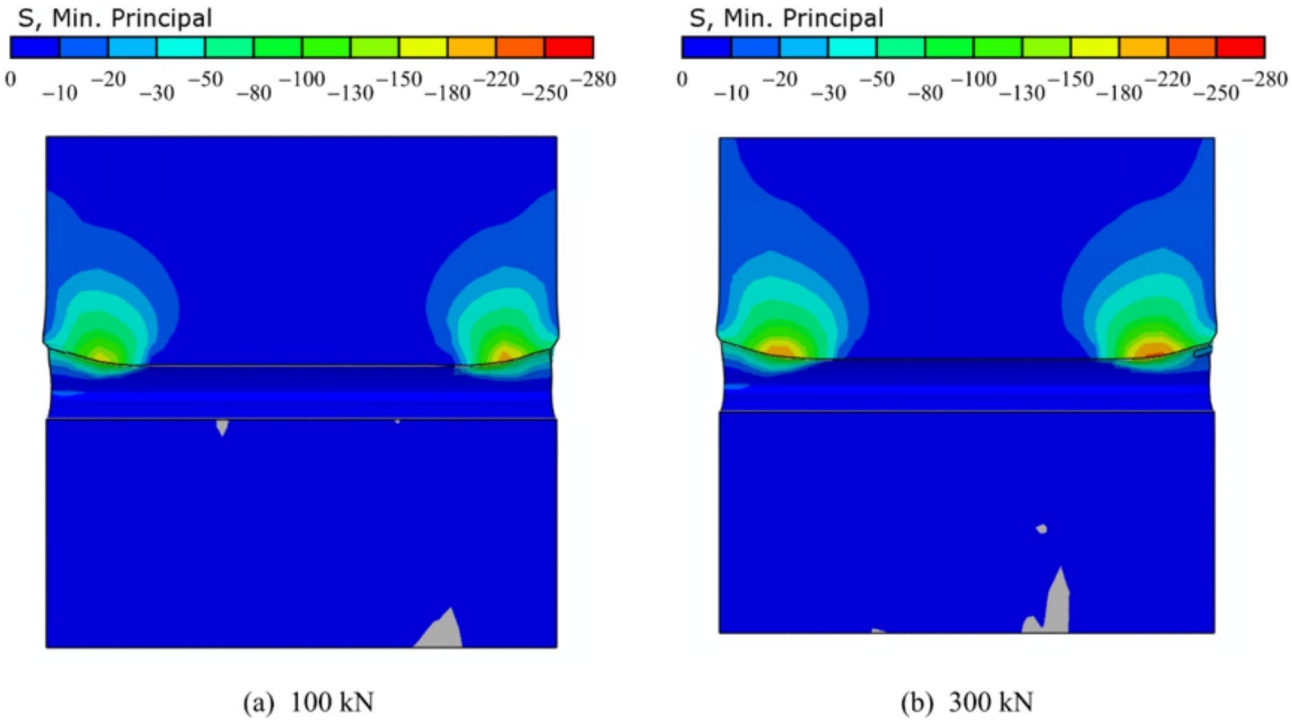

Fig. 15. Distribution of the minimum principal stress in the block under different pretension forces.

are shown in Fig. 27. It is apparent that at the same shear displacement, the higher the test block strength, the greater the bending angle at the shear plane position, and the more pronounced the bending deformation of the structure on both sides of the shear plane. At a shear displacement of 74 mm, the minimum principal stress of the middle test block for different test block strengths is compared in Fig. 28. It is clear that at the same shear displacement, the higher the test block strength, the greater the absolute value of the minimum principal stress at the core of the pressure-bearing area, and the smaller the range of the pressure-bearing area. This similarly suggests that an increase in test block strength results in a reduced plastic hinge extension distance for the same shear displacement. In their experimental study on the shear behavior of anchor bolts, Jalalifar et al.[30] also

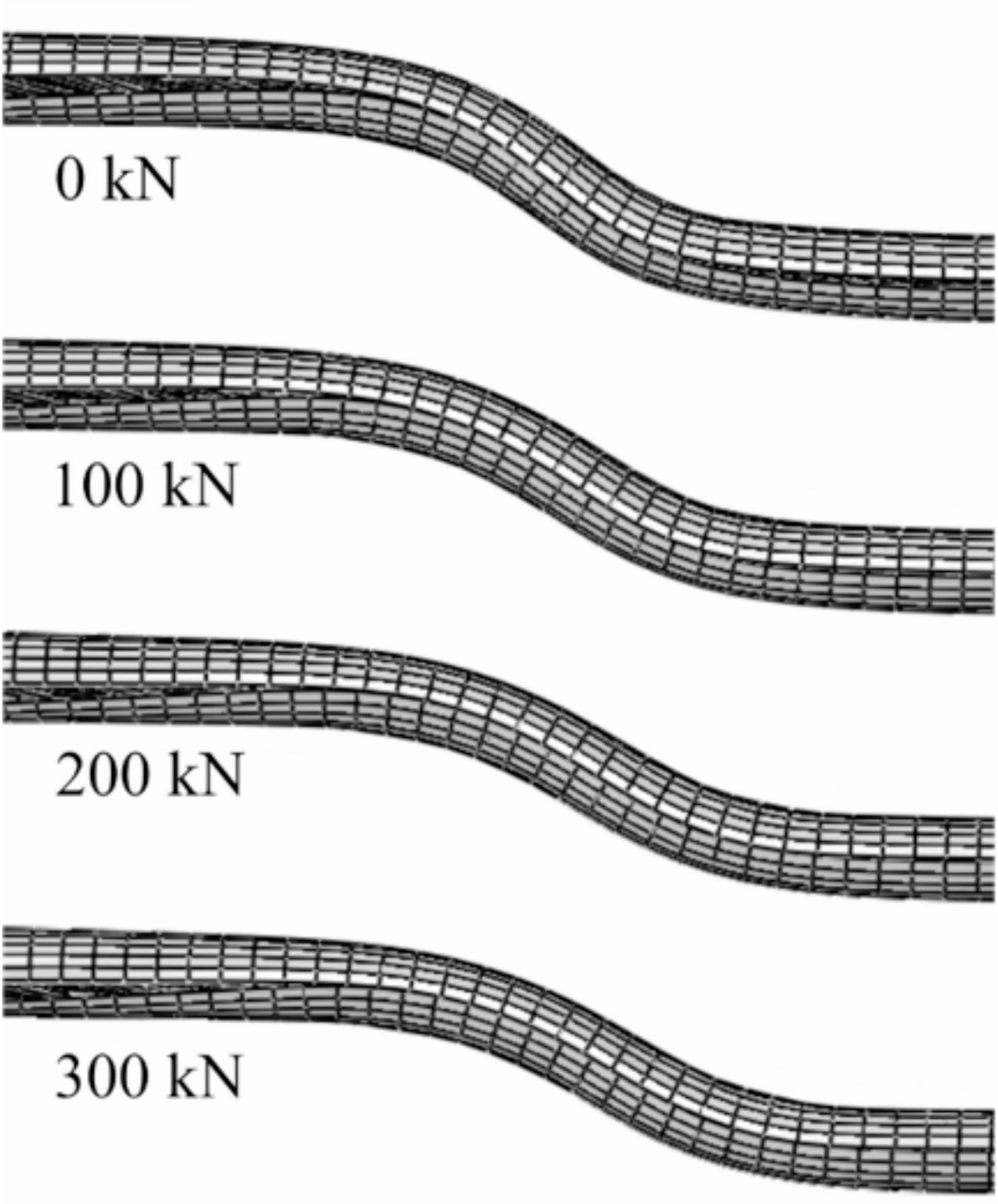

Fig. 16. Simulation results of structural deformation patterns under different pretension forces.

observed that as the strength of the test block increased, the propagation distance of the plastic hinge decreased. Notably, despite the different structural stiffness between the ACC and the anchor bolt, both exhibited similar deformation patterns under varying test block strengths, suggesting a universal nature of this phenomenon. As shown in Fig. 28a, with a test block strength of 20 MPa, the pressure-bearing areas on both sides of the test block extended and merged into a single entity.

At a shear displacement of 74 mm, the distribution of the Mises stress and maximum principal strain of plastic (Max principal strain of plastic, ε_1^{pl}) in the anchor cable under different test block strengths is shown in Fig. 29.

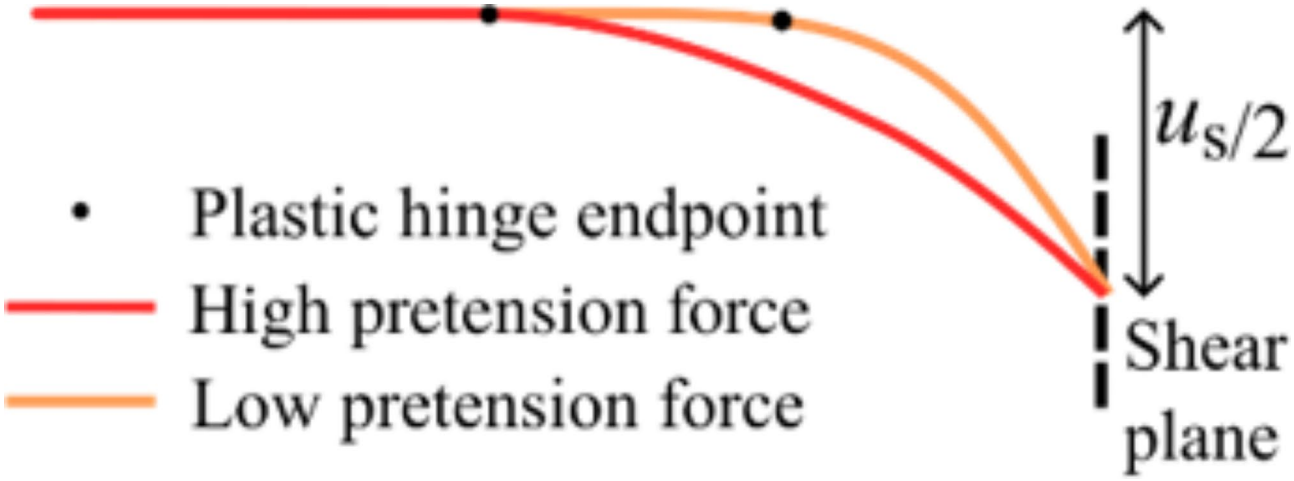

Fig. 17. Structural deformation patterns under different pretension forces.

As the test block strength increased, the range of higher Mises stress at the bending region and shear plane of the component underwent significant expansion, accompanied by a synchronized enlargement of the range of higher ε_1^{pl}. The larger ε_1^{pl} values were mainly distributed near the bending positions of the anchor cable and the shear plane. The shear displacement of the double shear system was composed of the bending deformation of the structure on both sides of the shear plane and the tensile deformation at the shear plane position. Combined with Fig. 28, it is noted that as the test block strength increases, the plastic hinge extension distance decreases for the same shear displacement, resulting in a reduced range of the deforming structure. Within this range, the bending and tensile deformations of the structure were more significant. The failure of the ACC typically occurred due to the rupture of the anchor cable, with the failure of metal wires occurring when the local strain reached the failure strain. As the test block strength increased, the deformation of the anchor cable at the shear plane position was more significant at the same shear displacement, meaning the local strain values were higher, leading to earlier rupture. Higher test block strength caused the bending angle of the structure to increase more rapidly, thereby increasing the rate of shear load rise. However, the reduction in break displacement decreased the peak shear load. The aggregate effect of these factors resulted in the peak shear load initially increasing and then decreasing with increasing test block strength, consistent with the results shown in Fig. 22a. Yang et al.[8] conducted double-shear tests on anchor cables using cement mortar with strengths of 30 MPa and 50 MPa as the test block materials. They similarly concluded that as the test block strength increased, the failure displacement decreased. However, the literature did not mention the characteristic that the peak shear load initially increases and then decreases with the test block strength due to the influence of shear stiffness.

Considering the influence of pre-tensioning on the mechanical response of ACC under shear loading and taking into account the strength and stiffness of the structure relative to the test block, the concept of "Relative Stiffness between Structure and Test Block" (RSSB) was proposed to characterize the relative relationship between the stiffness of the structure and the test block. From the perspective of test block-structure interaction, RSSB determined the deformation mode of the structure. The diameter of the anchor cable, the geometric structure of the anchor cable, the anchor cable material, and the C-shaped tube material influenced the stiffness of the structure. The material strength and size of the test block affected the stiffness of the test block. RSSB determined the evolution of the structure's bending and tensile deformation, thereby affecting the bending angle at the shear plane position, shear stiffness, peak shear load, and break displacement of the structure. The structural deformation under different RSSB values is compared in Fig. 30. Among them, $\mathrm{RSSB}_1 > \mathrm{RSSB}_2 > \mathrm{RSSB}_3 > \mathrm{RSSB}_4$.The larger the RSSB, the greater the plastic hinge extension distance at the same shear displacement, the smaller the bending angle at the shear plane position, and the smaller the maximum curvature of the structure.

In studying the shear resistance of support components, the distribution and evolution of the reaction force provided by the test block were crucial issues. For ACC, the test block applied a load to the structure through the contact force with the C-shaped tube. Using the "free body cut" feature in ABAQUS, the contact forces at different positions on the outer surface of the C-shaped tube were monitored. Under a pretension force of 200 kN and a test block strength of 40 MPa, the distribution of forces on the outer surface of the C-shaped tube at different shear displacements, after data smoothing, is represented in Fig. 31. The contact force on the C-shaped tube generally exhibited a single-peak distribution, with a double-peak distribution appearing only at the end of the shearing process. With increasing shear displacement, the maximum contact force rapidly increased and tended to stabilize. The range of the contact force distribution also expanded, and the position of the maximum contact force moved away from the shear plane.

The contact forces at different positions (with different z-coordinates) were monitored, and the results are shown in Fig. 32. When the plastic hinge had not yet extended to a given position, the contact force was zero. Subsequently, as the test block at that position was compressed, the contact force rapidly increased. With further compression deformation, the evolution of contact forces at different positions varied slightly. Some positions showed a slow, continuous increase; at others, the contact force decreased slightly before increasing again.

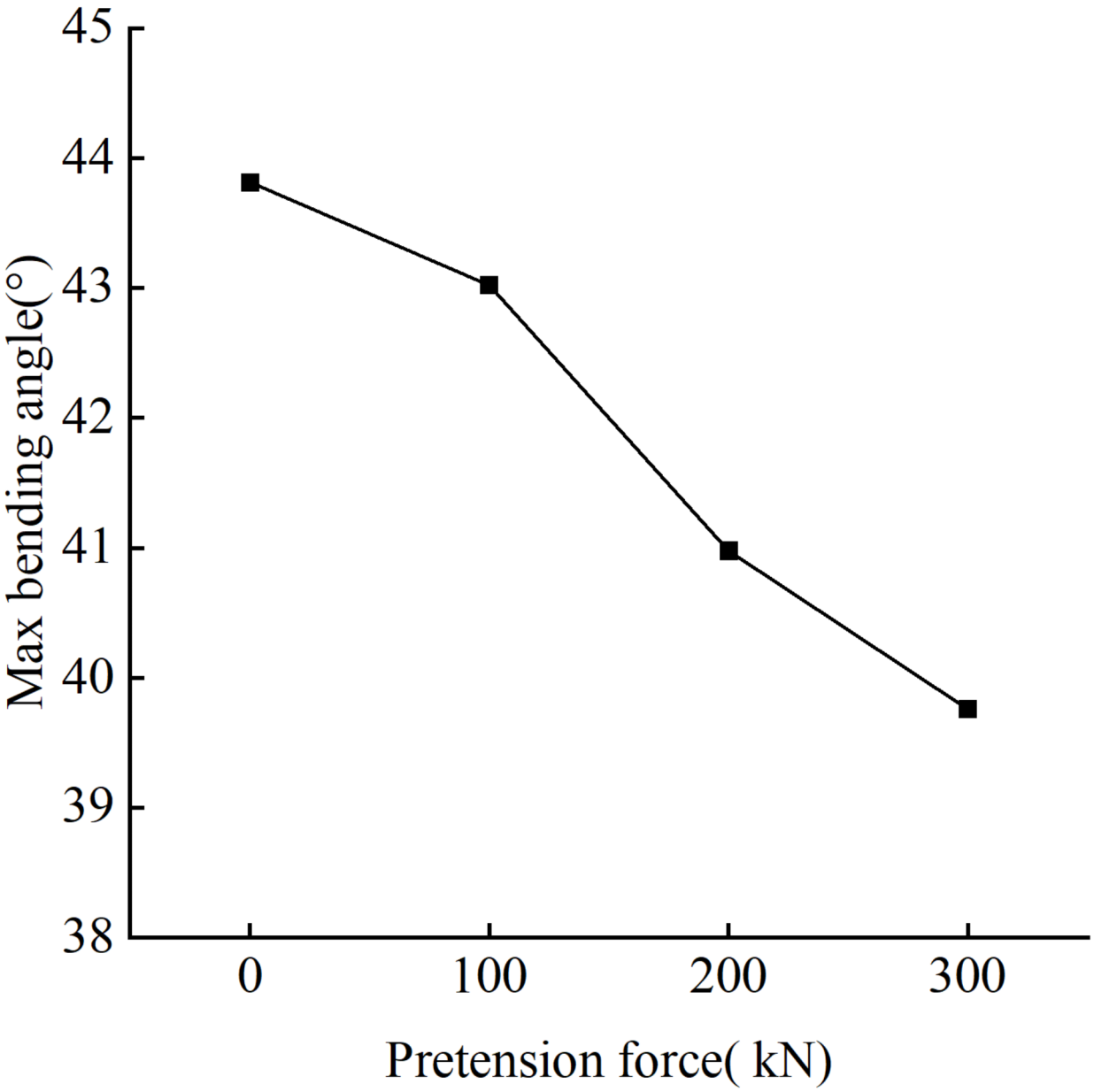

Fig. 18. Numerical results of the maximum bending angle of ACC under different pretension forces.

The specific evolution of contact forces was related to the test block's local damage evolution and compression deformation.

In past theoretical studies on the shear resistance of support components, two approaches were used to address the loads exerted by test blocks on structures. One approach treated the test block as the foundation and the structure as the foundation beam, applying loads to the structure through foundation stiffness and relative deformation. The other approach directly assumed the distribution of loads exerted by the test block on the structure and employed structural mechanics methods for solving. Literature[31,32] assumed a triangular load distribution; literature[33] divided the test block reaction force into elastic and plastic stages, with the elastic stage having a triangular distribution and the plastic stage having a rectangular distribution; literature[34] considered the force distribution as trapezoidal. Based on numerical simulation results, the force distribution was not a single form, as provided in Fig. 33. The contact force of the C-shaped tube exhibited a basic "single-peak" structure, with the peak position of the force moving away from the shear surface with increasing shear displacement, and the contact force at the shear surface position increasing. In the later stage of shearing, the force distribution formed a "double-peak" structure, with peaks forming locally where the compression of the test block was significant.

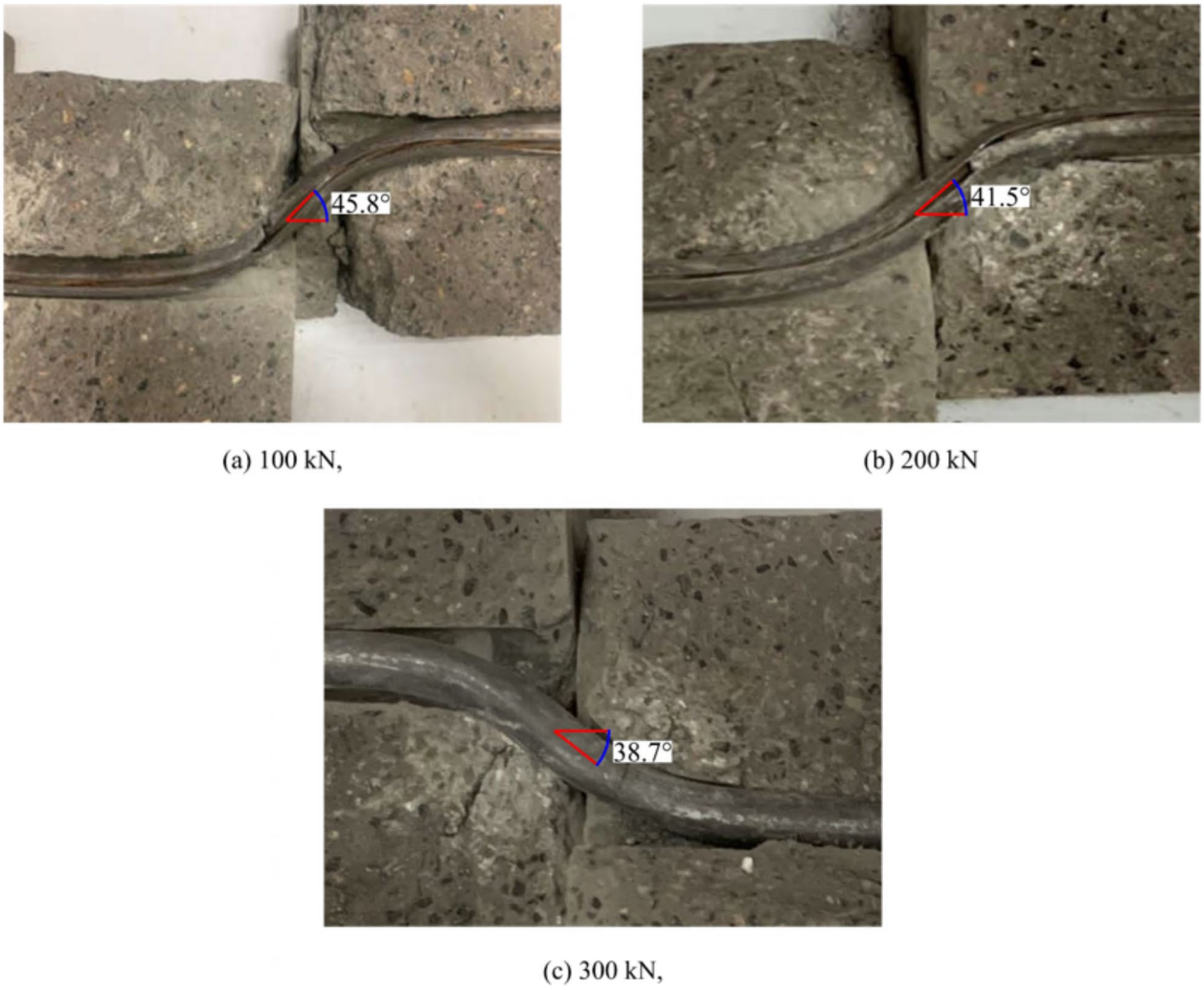

Fig. 19. Experimental results of the maximum bending angle of ACC under different pretension forces[29].

Different test block strengths corresponded to the evolution of the maximum contact force exerted on the C-shaped pipes, as illustrated in Fig. 34. With an increase in test block strength, the maximum contact force noticeably increased. Moreover, during the early and middle stages of shearing, the maxcontact force exerted by the high-strength test blocks on the C-shaped pipes exceeded that of the low-strength ones.

At a shearing displacement of 30 mm, the comparison of the contact force distribution under different test block strengths is depicted in Fig. 35. The contact force distribution under different test block strengths adheres to the pattern illustrated in Fig. 33. Higher test block strengths resulted in larger maximum contact force values and a smaller non-zero range of contact force. Conversely, lower test block strengths mobilized a more extensive range to bear the load. The distribution and evolution of contact force on the C-shaped pipes essentially represented the reactive forces exerted by the test blocks on the structure, significantly influencing the formation of structural bending morphology.

Conclusion

(1) In order to investigate the shear mechanical response of ACC and the influence mechanism of pre-tensioning force and test block strength on the shear resistance of ACC, a refined numerical analysis model of the actual seven-strand structural steel strand anchor cable combined with C-shaped pipes was original established using ABAQUS software.

(2) Successfully proves the high correlation between peak shear loads and different pretension forces. The increase in pre-tensioning force decreased the peak shear load and rupture displacement of ACC. With high pre-tensioning force, the structure exhibited higher bending stiffness, and the test block strength was mobilized earlier, leading to earlier local failure of the test block. Consequently, the bending angle decreased at the same shear displacement, albeit with a slight difference. Under high pre-tensioning force, the initial shear stiffness of the system was higher, mainly influenced by the axial force component. Under low pre-tensioning force, the elongation of the anchor cable at the shear interface was smaller at the same shear

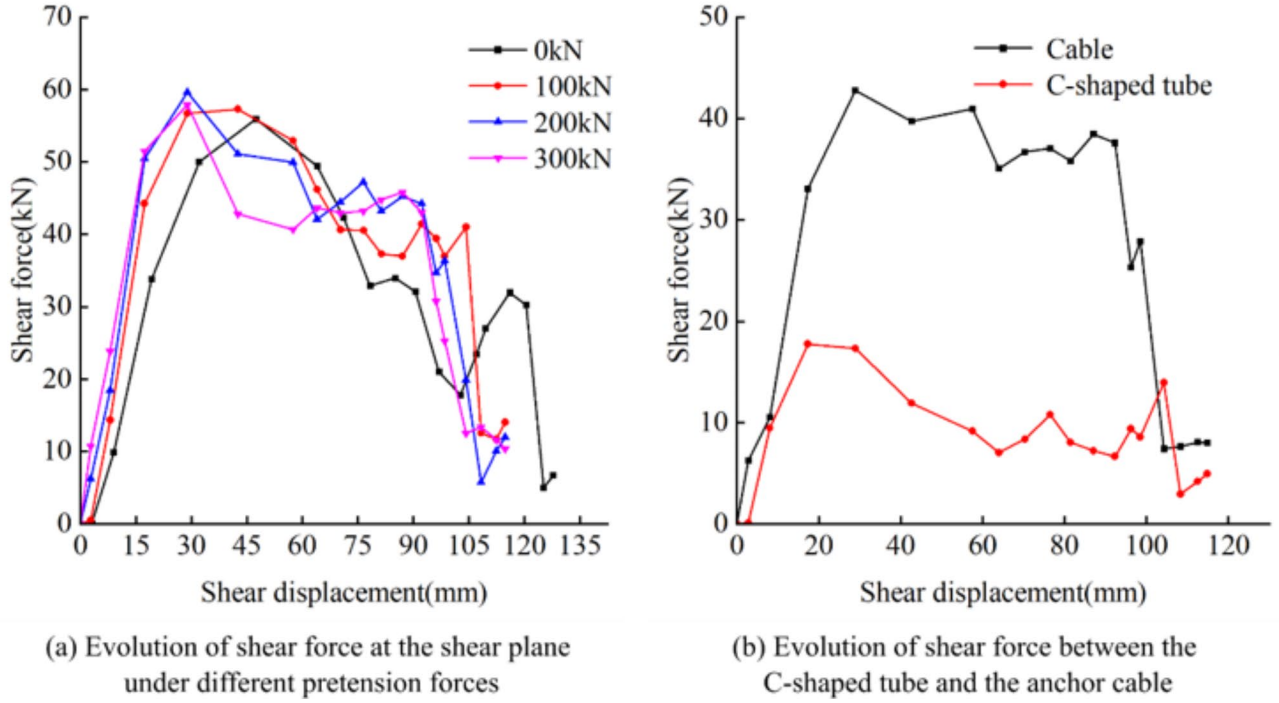

(a) Evolution of shear force at the shear plane under different pretension forces

(b) Evolution of shear force between the C-shaped tube and the anchor cable

Fig. 20. The evolution and distribution of shear force at the ACC's shear plane under different pretension forces.

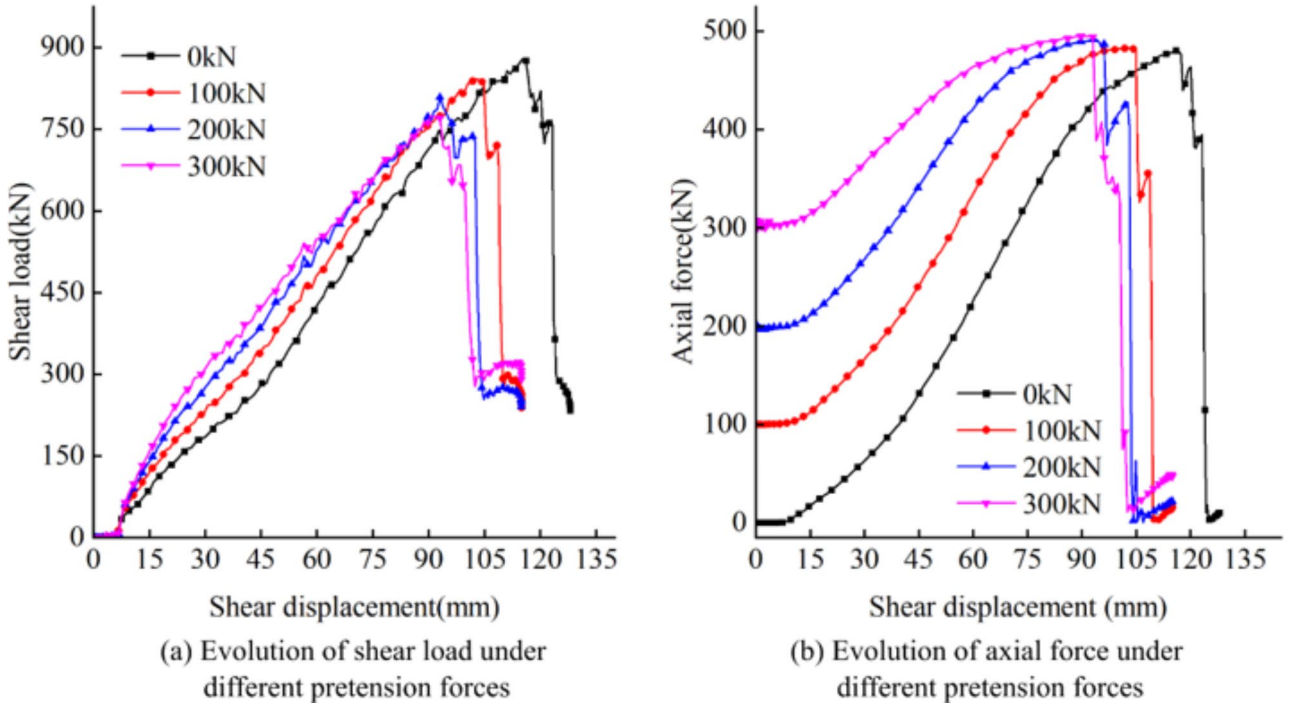

(a) Evolution of shear load under different pretension forces

(b) Evolution of axial force under different pretension forces

Fig. 21. The evolution of shear load and axial force of ACC under different pretension forces.

displacement, resulting in a larger ultimate rupture displacement. Additionally, under low pre-tensioning force, the bending angle of ACC increased rapidly in the later stages of shearing, and the rupture displacement of ACC was greater. The combined effect of these factors led to a larger bending angle at the shear interface rupture under low pre-tensioning force.

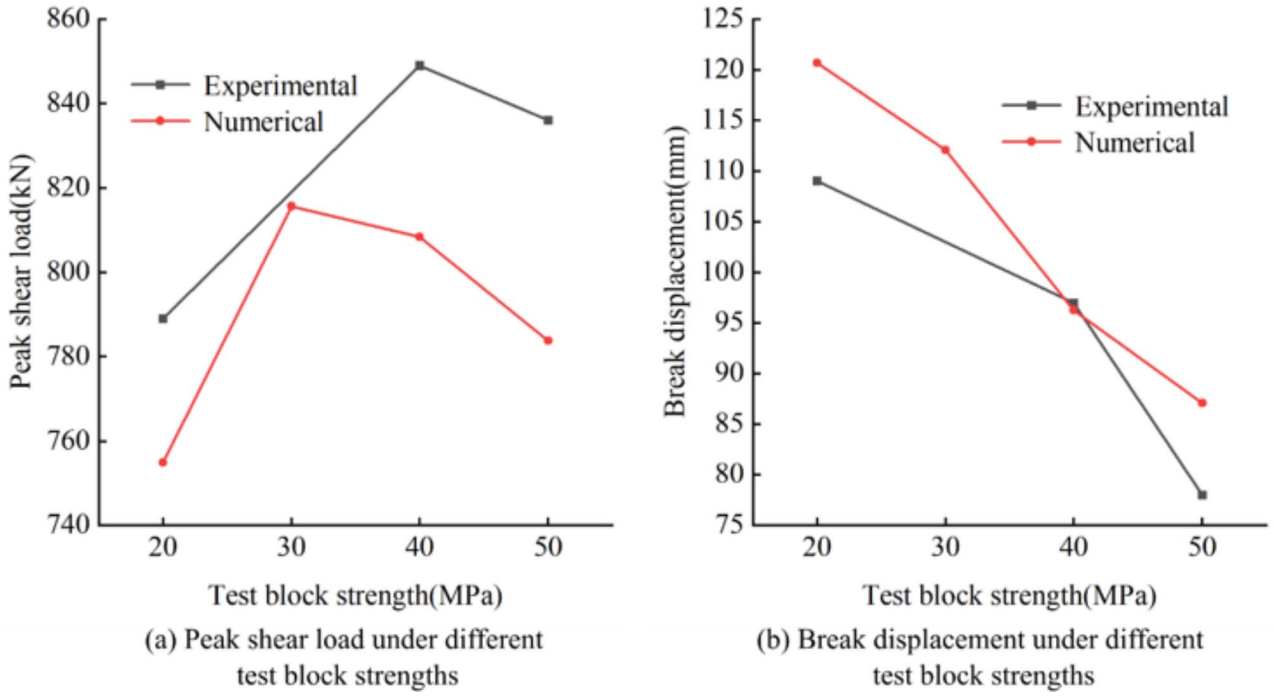

Fig. 22. Peak shear load and break displacement of ACC under different test block strengths.

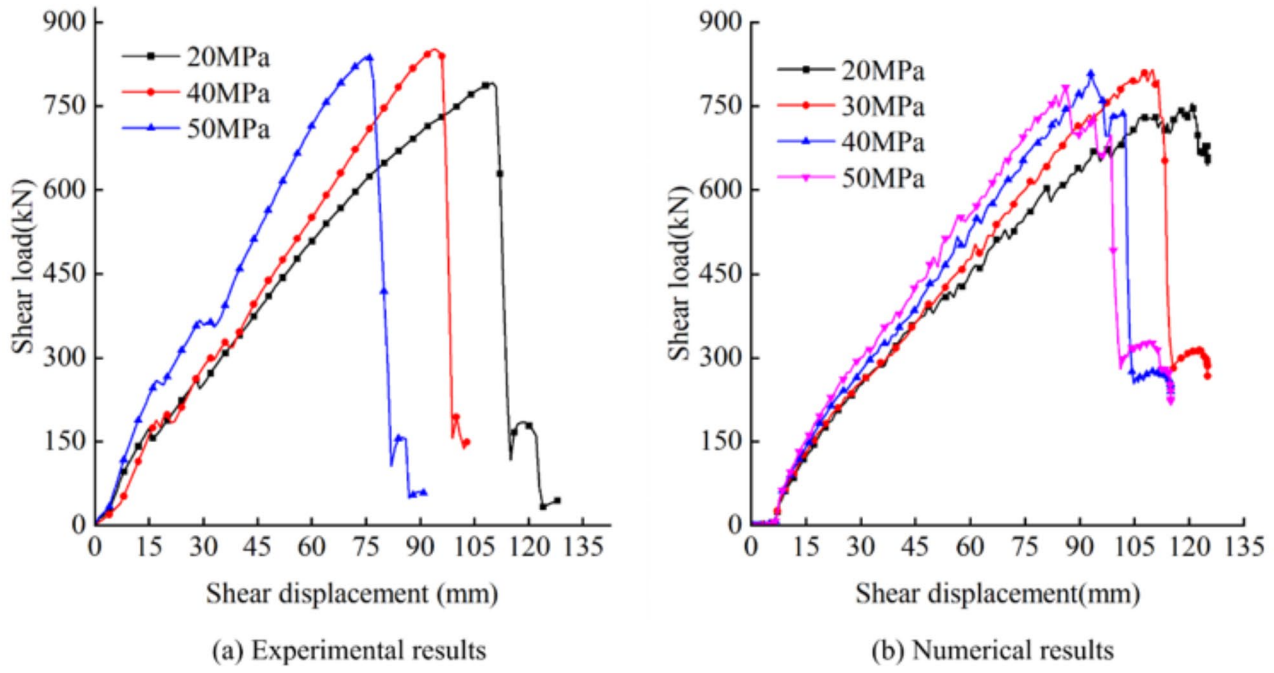

Fig. 23. Numerical simulation results and experimental results of ACC's shear load evolution at different test block strengths.

(3) As the test block strength increased, the bending angle at the shear plane position of the structure grew faster, which is also the primary source of ACC's high shear stiffness under high test block strength. The combined effect of smaller break displacement and greater shear stiffness at high test block strength caused the peak shear load to increase and then decrease with increasing test block strength.
(4) The deformation pattern of the structure was controlled by the "Relative Stiffness between Structure and Test Block" (RSSB). A higher RSSB corresponded to a greater plastic hinge extension distance under the

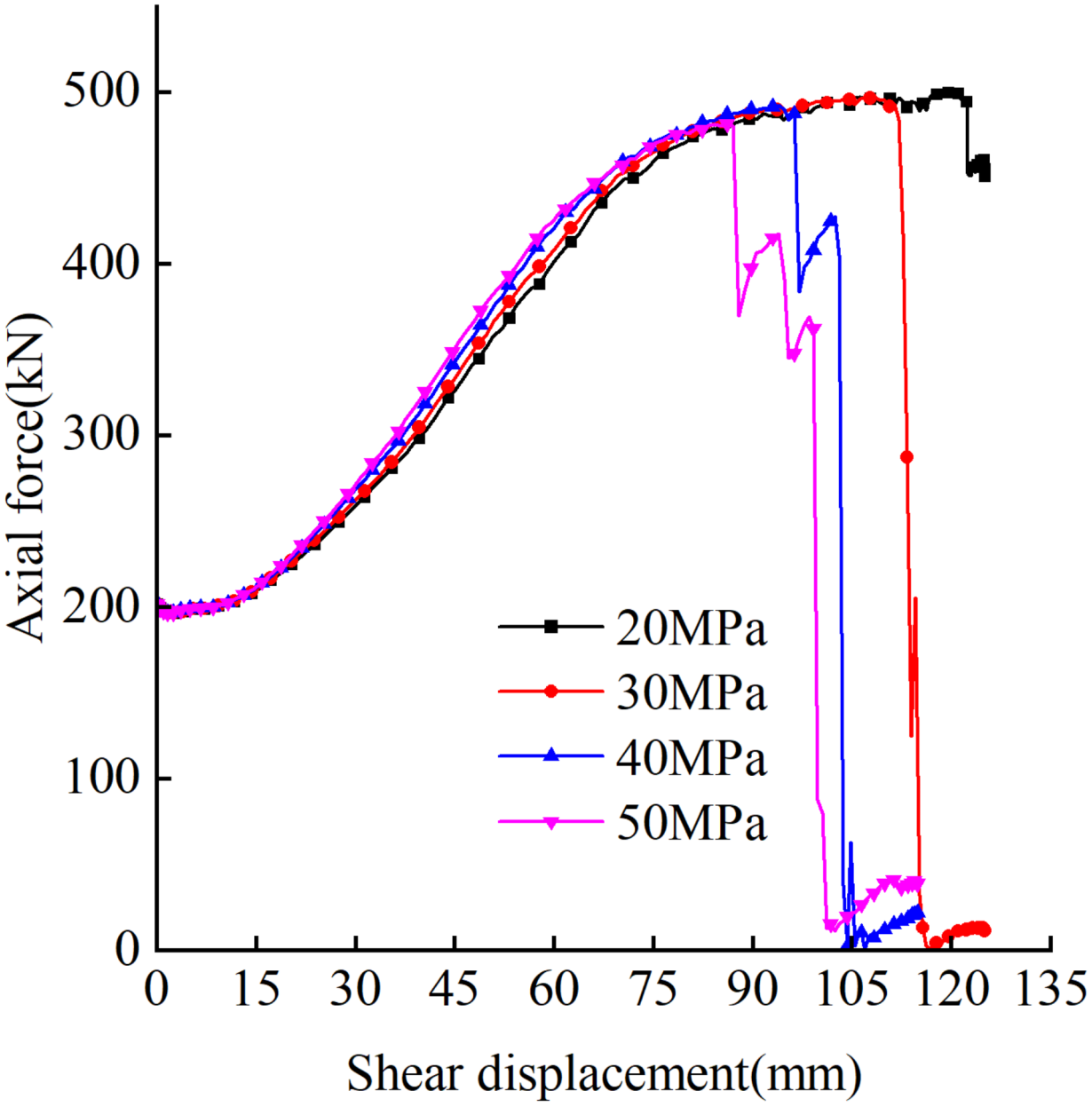

Fig. 24. Evolution of axial force in ACC under different test block strengths.

same shear displacement, resulting in a smaller bending angle at the shear interface and a smaller maximum curvature of the structure.

(5) Overall, the contact force of the C-shaped pipe exhibited a "single-peak" distribution. With the increase in shear displacement, the peak position of the contact force moved away from the shear surface direction. The maximum contact force increased rapidly with the increase in shear displacement and then remained relatively stable. In the late shear stage, the contact force of the C-shaped pipe exhibited a "double-peak" distribution.

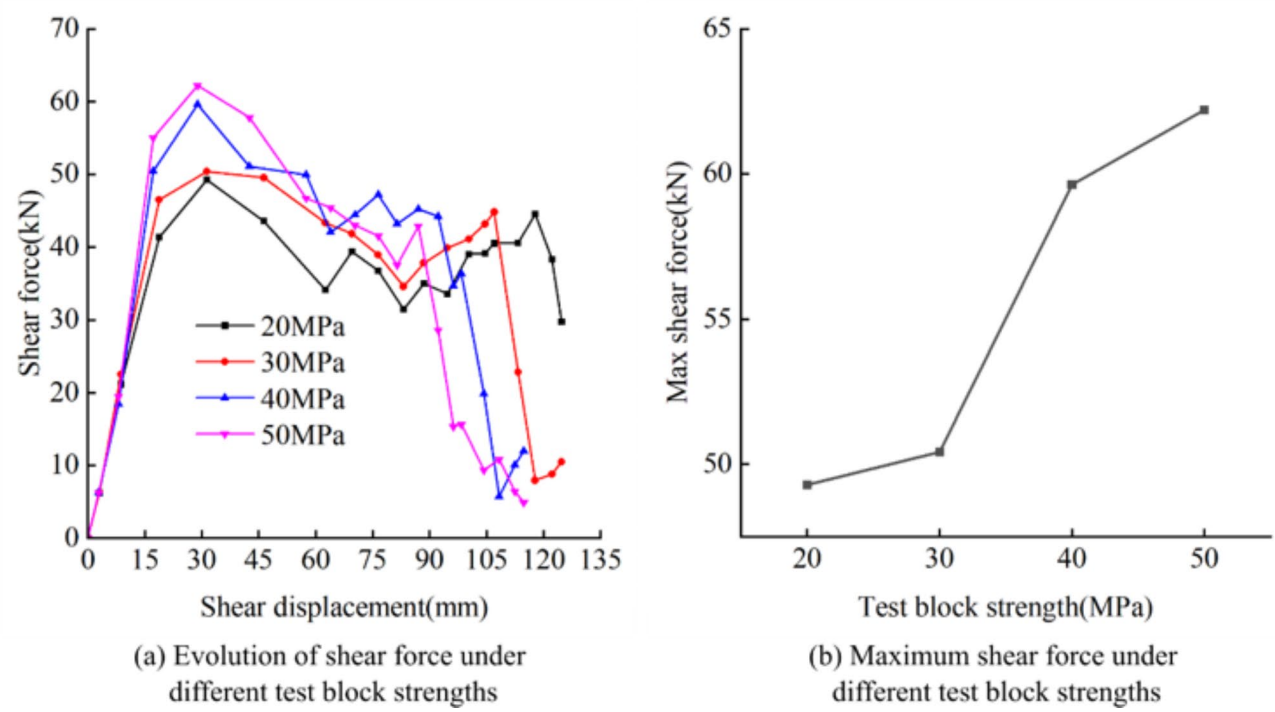

Fig. 25. Evolution of structural shear force and maximum shear force under different test block strengths.

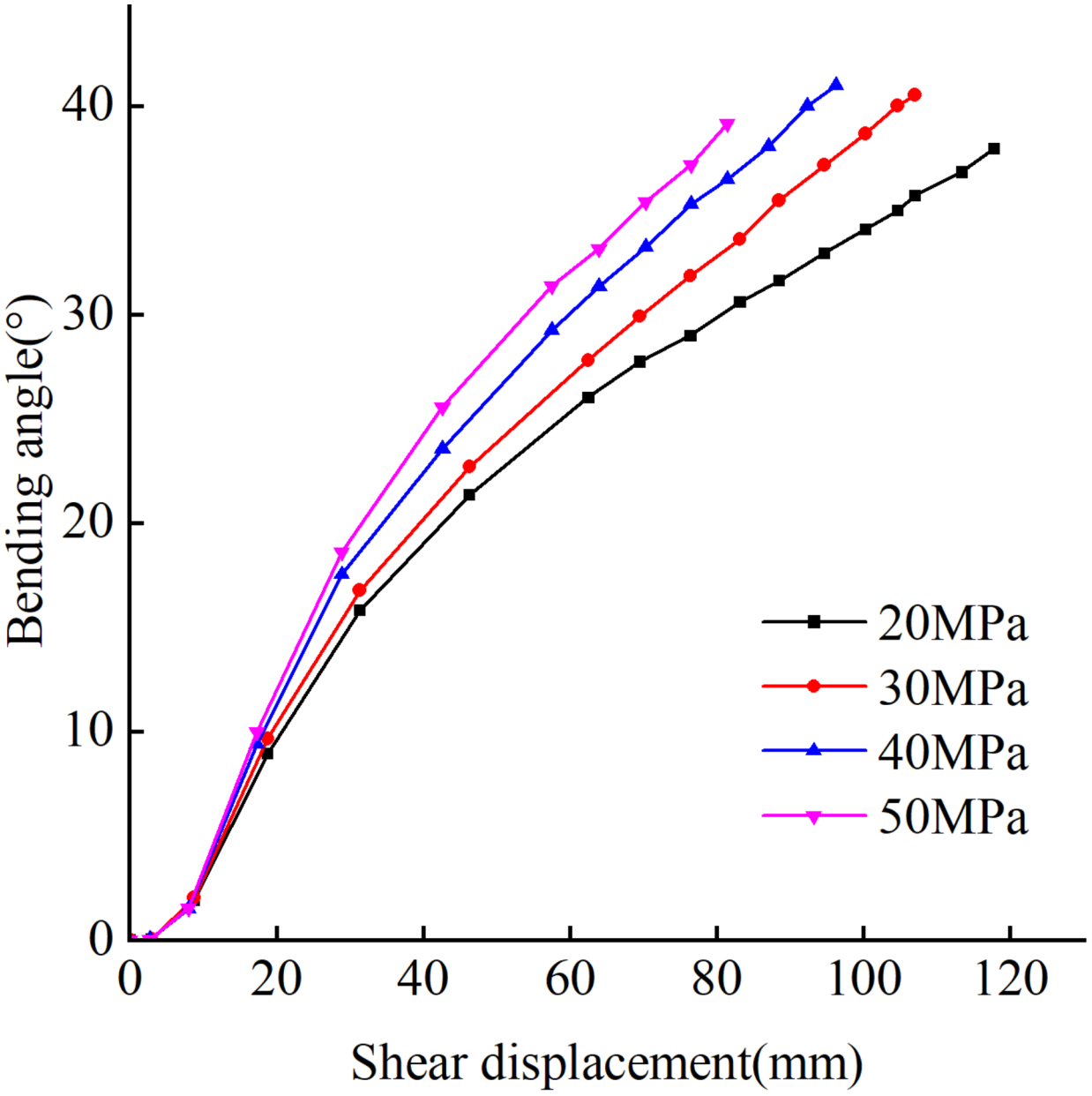

Fig. 26. Evolution of structural bending angle under different test block strengths.

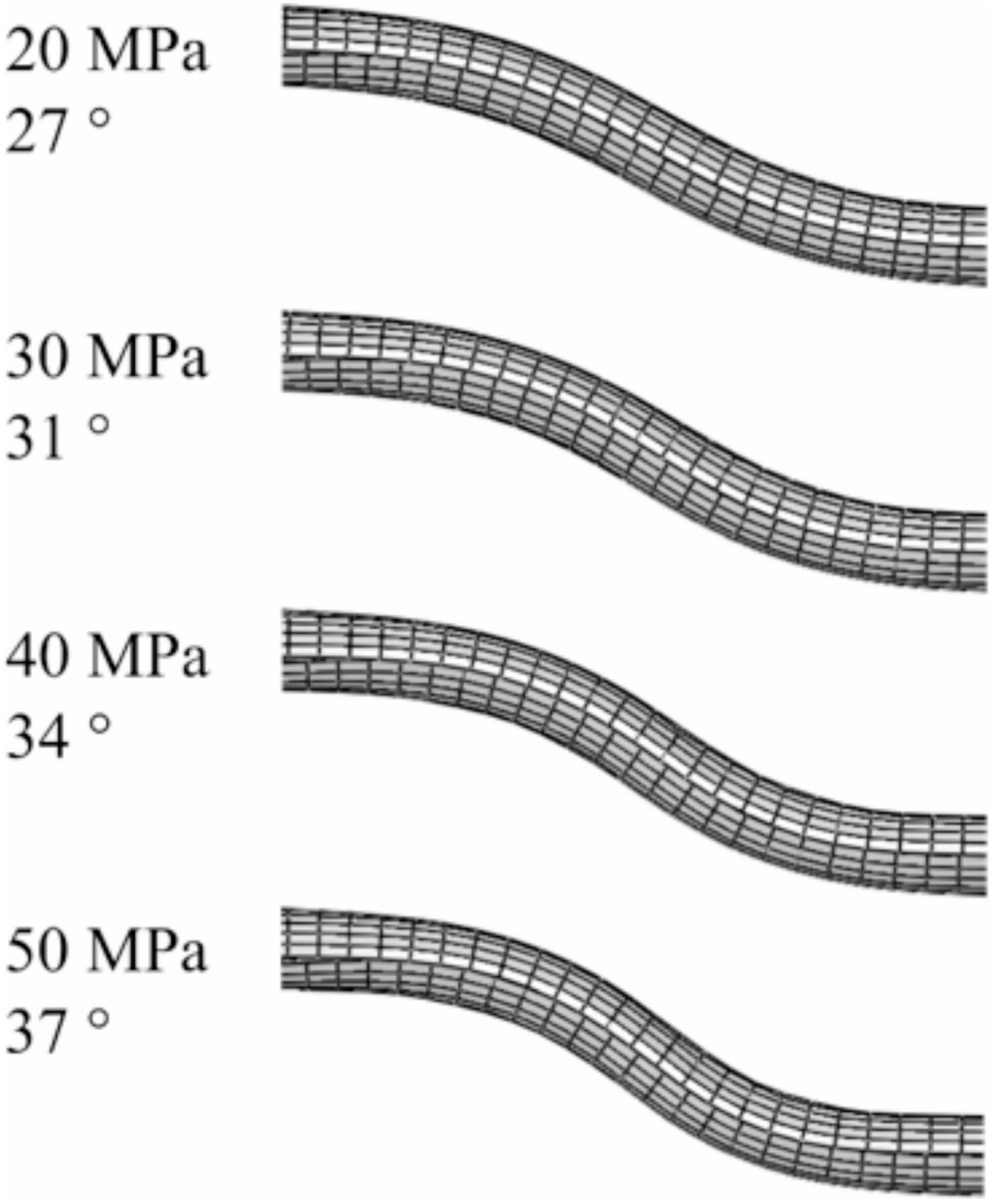

Fig. 27. Comparison of structural bending angles under different test block strengths (with a shear displacement of 74 mm).

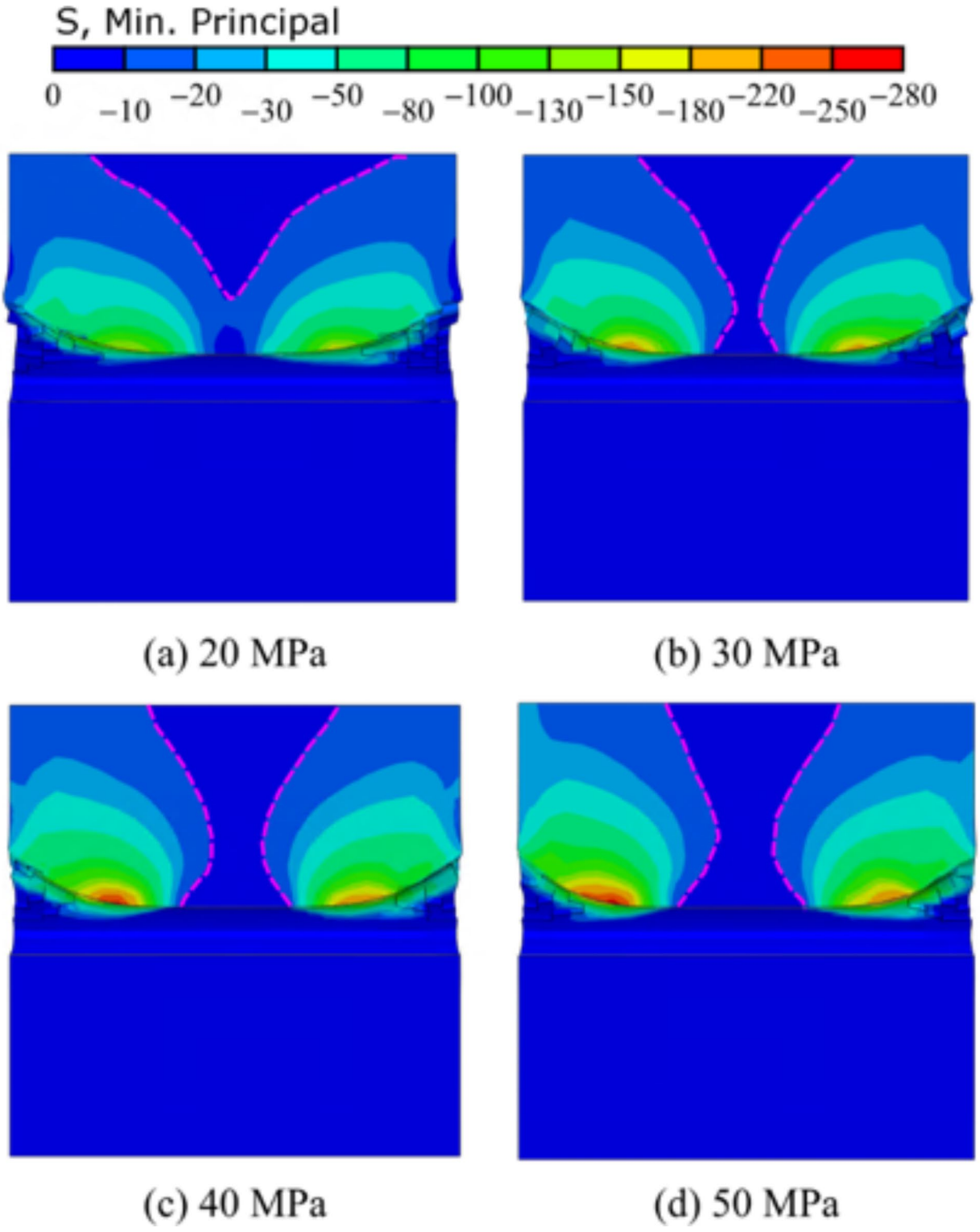

Fig. 28. Comparison of the block's min principal stress at a shear displacement of 74 mm under different test block strengths.

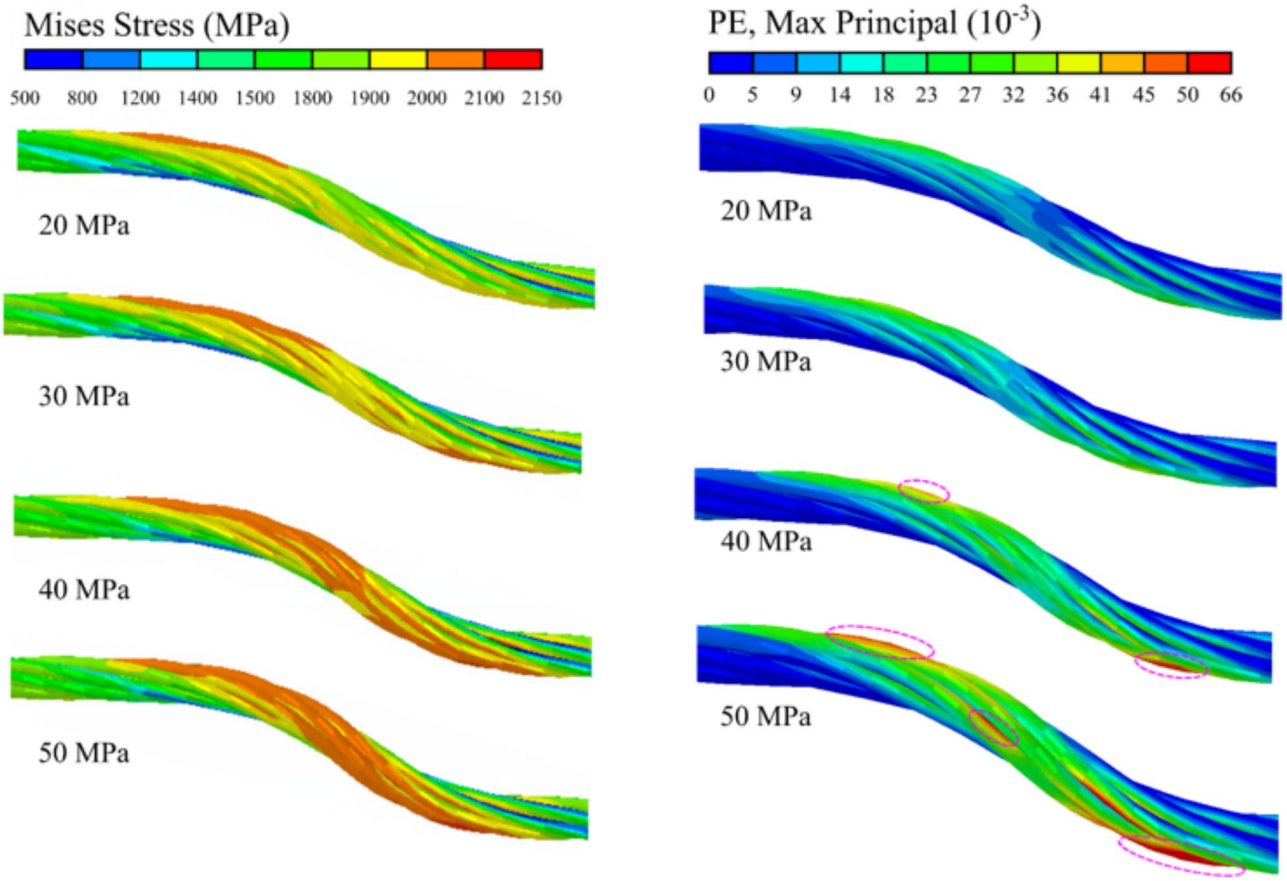

Fig. 29. Comparison of the maximum principal plastic strain and Mises stress in the anchor cable at a shear displacement of 74 mm under different test block strengths.

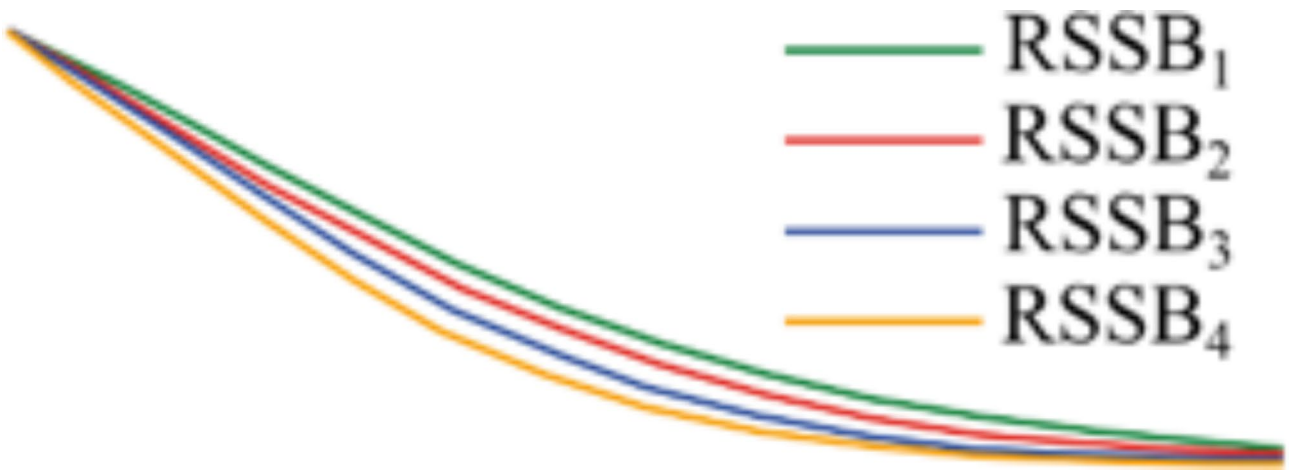

Fig. 30. Schematic representation of structural deformation under different RSSB.

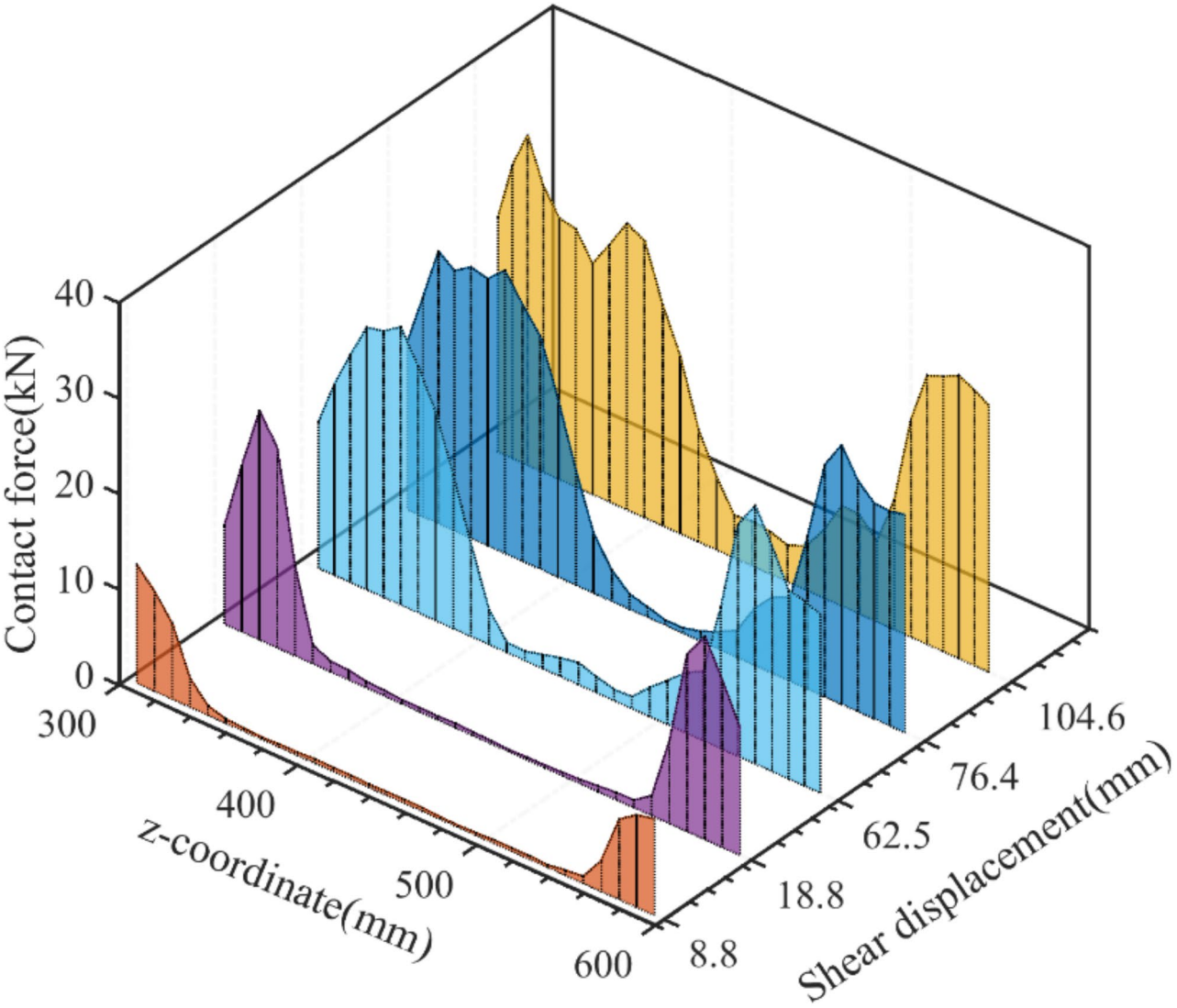

Fig. 31. Distribution of contact force on the C-shaped tube under different shear displacements.

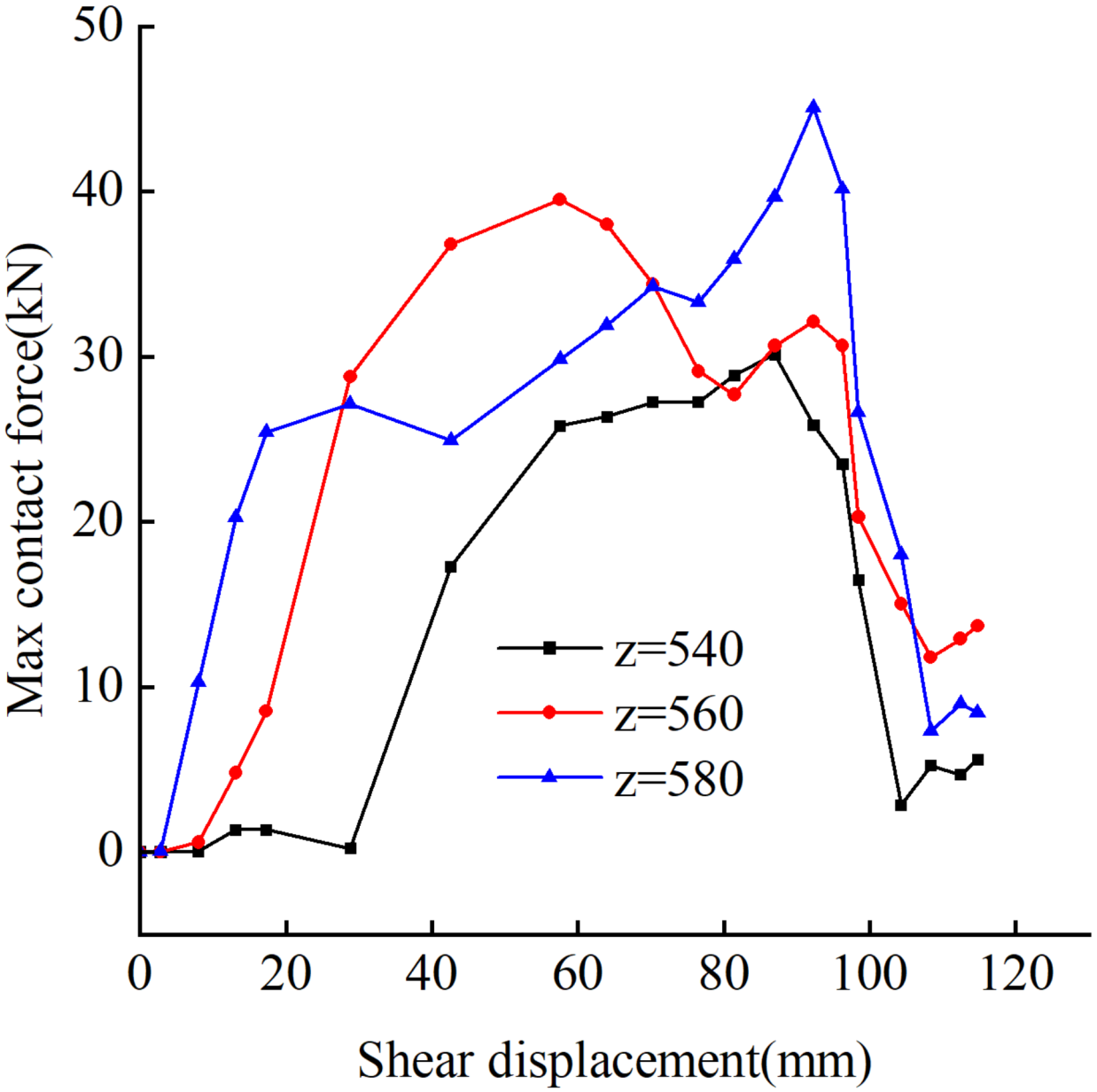

Fig. 32. Evolution of contact force at various locations on the C-shaped tube.

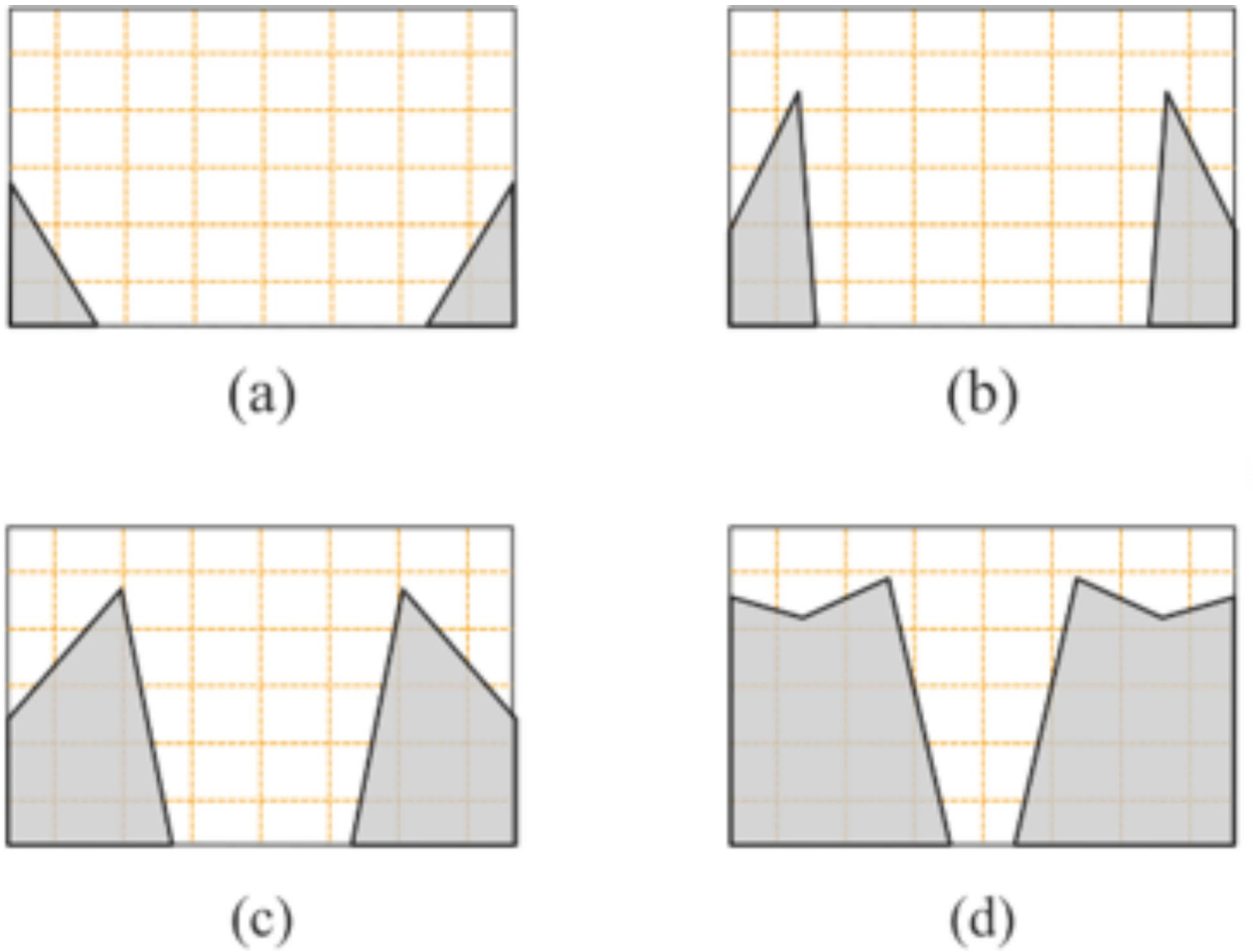

Fig. 33. Schematic representation of the evolution of contact force on the C-shaped tube.

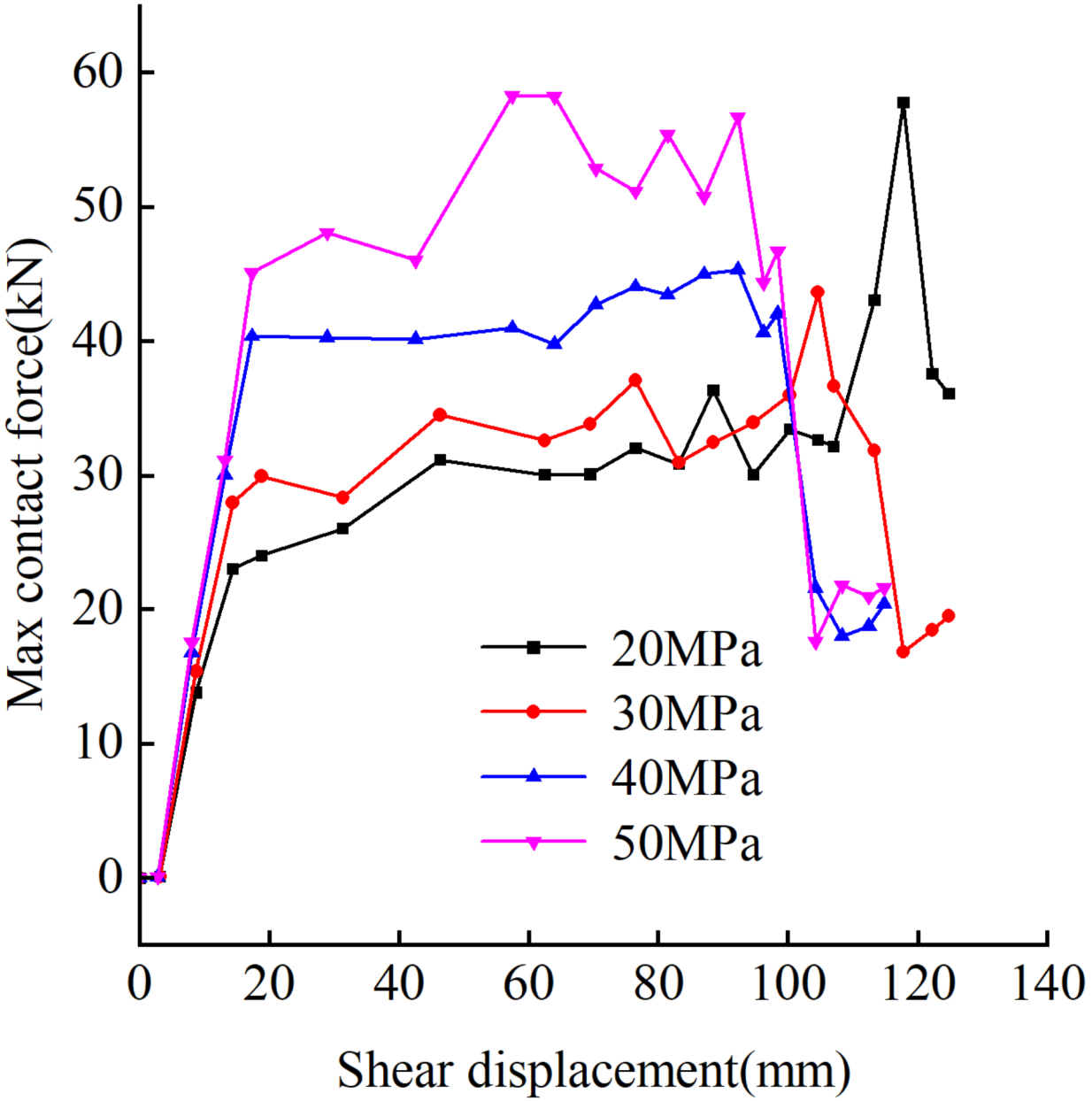

Fig. 34. Evolution of the maximum contact force on the C-shaped tube under different test block strengths.

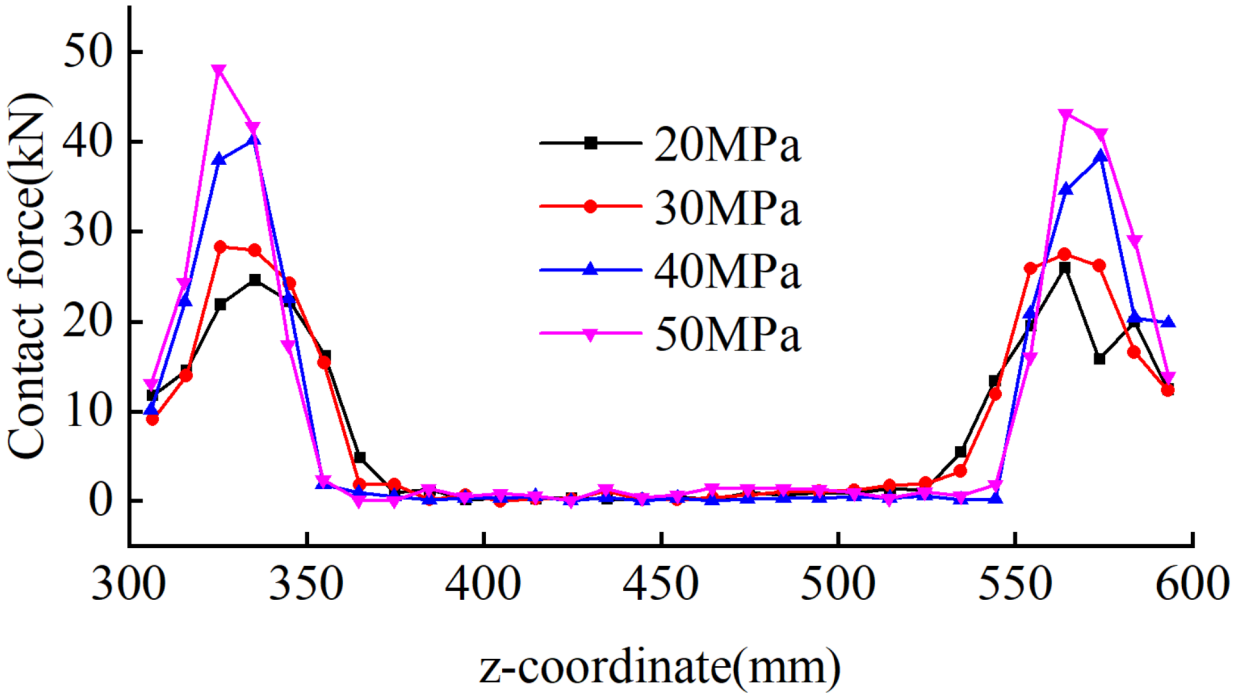

Fig. 35. Distribution of contact force on the C-shaped tube under different test block strengths (with a shear displacement of 30 mm).

Data availability

The datasets used and analyzed during the current study are available from the corresponding author on reasonable request.

Received: 25 June 2024; Accepted: 23 September 2024
Published online: 02 October 2024

References

1. Li, Y. L. *Deformation Instability Mechanism and Supporting Technology of large-section coal Roadway with Layered roof in Zhaozhuang coal mine* (China university of mining and technology (Beijing), 2017).
2. Jiang, Q., Feng, X. T., Cui, J. & Li, S. J. Failure mechanism of Unbonded Prestressed thru-Anchor Cables: in situ investigation in large Underground Caverns. *Rock Mech. Rock Eng.* **48**, 873–878 (2015).
3. Li, P., Lai, X. P. & Shen, Y. X. Breaking mechanism of anchor cable in layered roof roadway. *J. Xi'an Univ. Sci. Technol.* **41**, 608–615 (2021).
4. Shan, R. L., Tao, Y. & Kong, X. S. *Anchor Cable with C-shaped tube Capable of Withstanding Lateral Shear Forces* (CN103967509A, 2014).
5. Shan, R. L. et al. Research progress of coal roadway support technology at home and abroad. *Chin. J. Rock Mech. Eng.* **38**, 2377–2403 (2019).
6. Kang, H. P., Yang, J. H. & Jiang, P. F. Tests and analysis on mechanical properties for cable bolts. *Coal Sci. Technol.* **43**, 29–33 (2015).
7. Aziz, N. et al. An experimental study on the Shear performance of fully encapsulated Cable bolts in single Shear Test. *Rock Mech. Rock Eng.* **51**, 2207–2221 (2018).
8. Yang, R. S. et al. Experimental study of shear mechanical properties of prestressed cable bolts. *J. China Univ. Min. Technol.* **47**, 1166–1174 (2018).
9. Chen, W. Q. et al. Analysis of axial and transverse effects of rock bolt during shearing process. *Rock Soil Mech.* **36**, 143–148 (2015).
10. Liu, Q. S. et al. Experimental study and mechanism analysis of influence of bolt anchoring on shear properties of jointed rock mass. *Rock Soil Mech.* **38**, 27–35 (2017).
11. Wang, X. G., Zhou, J. J., Jia, Z. X., Zhao, Y. F. & Liu, L. P. Shear tests on bolted joint planes. *Rock Soil Mech.* **37**, 250–256 (2016).
12. Song, Y., Fan, B. & Wang, H. P. Research on shear mechanics model of anchored-jointed rock mass considering normal stress and rock strength. *Chin. J. Rock Mech. Eng.* **42**, 1325–1335 (2023).
13. Zhang, S. B. et al. Experimental study on the shear behaviors of bolted rock joints reinforced with BFRP bars. *Chin. J. Rock Mech. Eng.* **41**, 712–724 (2022).
14. Wang, K., Zhao, Y., Hu, Z. & Nie, Y. Shear Test of Pre-stressed Anchor Block and fracture mechanism analysis of Anchor Cable. *Rock Mech. Rock Eng.* **56**, 589–601 (2022).
15. Tahmasebinia, F., Yang, A., Feghali, P. & Skrzypkowski, K. Structural Evaluation of Cable Bolts under Static Loading. *Appl. Sci. Basel* **13**, 1326 (2023).
16. Tahmasebinia, F., Yang, A., Feghali, P. & Skrzypkowski, K. A Numerical Investigation to calculate Ultimate Limit State Capacity of Cable bolts Subjected to Impact Loading. *Appl. Sci.* **13**, 15 (2022).
17. Ma, S. Q., Zhao, Z. Y., Peng, J. & Gui, Y. L. Analytical modeling of shear behaviors of rockbolts perpendicular to joints. *Constr. Build. Mater.* **175**, 286–295 (2018).
18. Jiang, Y. J. et al. Experimental study on shear characteristics of bolted rock joints under constant normal stiffness boundary conditions. *Chin. J. Rock Mech. Eng.* **40**, 663–675 (2021).
19. Shan, R. L. et al. Research on the anchor cable combined with the C-shaped tube and the mechanical properties. *Rock Soil Mech.* **43**, 602–614 (2022).
20. Tong, X., Shan, R., Liu, N., Liu, D. & Wei, Y. H. Experimental study on the shear performance of an anchor cable with a C-shaped tube anchored flat structural plane. *Sci. Rep.* **13**, 797 (2023).
21. Shan, R. L., Song, W., Zhang, S. P., Liu, S. & Liang, J. Q. Precise finite element analysis of shear mechanical response of anchor cable with C-shaped tube in roadway support. *Chin. J. Rock Mech. Eng.* 1–19. https://doi.org/10.13722/j.cnki.jrme.2023.0835
22. Shan, R. et al. Experimental study on the shear mechanical properties of anchor cable with C-shaped tube. *Sustainability* **14**, 9616 (2022).
23. Shan, R. et al. Behavior of anchor cable bolts with c-shaped tube and cable bolts in shear test. *AIP Adv.* **12**, 105006 (2022).
24. Shan, R. L. et al. Research on the new technology of anchor cable with C-shaped tube support and its application in deep large deformation roadway. *J. Min. Sci. Technol.* **8**, 39–49 (2023).
25. Yu, Z. W. & Ding, X. F. Unified calculation method of compressive mechanical properties of concrete. *J. Build. Struct.* **24**, 41–46 (2003).
26. Ding, X. F. & Yu, Z. W. Unified calculation method for the tensile mechanical properties of concrete. *J. Hust*. **21**, 29–34 (2004).
27. Liu, C. H. & Li, Y. Z. Research progress in bolting mechanism and theories of fully grouted bolts in jointed rock masses. *Chin. J. Rock Mech. Eng.* **37**, 1856–1872 (2018).
28. Chen, Z., Yu, Y., Wang, X., Wu, X. & Liu, H. Experimental research on bending performance of structural cable. *Constr. Build. Mater.* **96**, 279–288 (2015).
29. Zhang, S. P. *Study on the Theory and Technology of Anchor Cable with C-shaped tube Structure Support in deep Roadway* (China university of mining and technology (Beijing), 2022).
30. Jalalifar, H. & Aziz, N. Analytical Behaviour of bolt–joint intersection under lateral loading conditions. *Rock Mech. Rock Eng.* **43**, 89–94 (2010).
31. Liu, C. H. & Li, Y. Z. Analytical Study of the mechanical behavior of fully grouted bolts in Bedding Rock Slopes. *Rock Mech. Rock Eng.* **50**, 2413–2423 (2017).
32. Wang, F. L., Liu, C. H. & Gong, Z. Mechanisms of bolt support for bedding rock slopes. *Chin. J. Rock Mech. Eng.* **33**, 1465–1470 (2014).
33. Li, X., Nemcik, J., Mirzaghorbanali, A., Aziz, N. & Rasekh, H. Analytical model of shear behaviour of a fully grouted cable bolt subjected to shearing. *Int. J. Rock Mech. Min. Sci.* **80**, 31–39 (2015).
34. Pellet, F. & Egger, P. Analytical model for the mechanical behaviour of bolted rock joints subjected to shearing. *Rock Mech. Rock Eng.* **29**, 73–97 (1996).

Author contributions

R.S.: Methodology, Resources, Funding acquisition. W.S.: Conceptualization, Methodology, Validation, Investigation, Formal analysis, Writing—original draft. S.Z.: Investigation. X.T.: Investigation. J.L.: Investigation.

Declarations

Competing interests
The authors declare no competing interests.

Additional information
Correspondence and requests for materials should be addressed to W.S.

Reprints and permissions information is available at www.nature.com/reprints.

Publisher's note Springer Nature remains neutral with regard to jurisdictional claims in published maps and institutional affiliations.

Open Access This article is licensed under a Creative Commons Attribution-NonCommercial-NoDerivatives 4.0 International License, which permits any non-commercial use, sharing, distribution and reproduction in any medium or format, as long as you give appropriate credit to the original author(s) and the source, provide a link to the Creative Commons licence, and indicate if you modified the licensed material. You do not have permission under this licence to share adapted material derived from this article or parts of it. The images or other third party material in this article are included in the article's Creative Commons licence, unless indicated otherwise in a credit line to the material. If material is not included in the article's Creative Commons licence and your intended use is not permitted by statutory regulation or exceeds the permitted use, you will need to obtain permission directly from the copyright holder. To view a copy of this licence, visit http://creativecommons.org/licenses/by-nc-nd/4.0/.

© The Author(s) 2024